

1  
2  
3  
4  
5  
6  
7 **Quantification of hydrologic impacts of climate change in a Mediterranean**  
8 **basin in Sardinia, Italy, through high-resolution simulations**  
9

10  
11 Monica Piras<sup>1,2</sup>, Giuseppe Mascaro<sup>1,2,3,\*</sup>, Roberto Deidda<sup>1,2</sup> and Enrique R. Vivoni<sup>3,4</sup>  
12  
13

14  
15 1. Dipartimento di Ingegneria Civile, Ambientale ed Architettura  
16 Università degli Studi di Cagliari  
17 Cagliari, Italy  
18

19 2. Consorzio Interuniversitario Nazionale per la Fisica dell'Atmosfera e dell'Idrosfera  
20 Tolentino, Italy  
21

22 3. School of Sustainable Engineering and the Built Environment  
23 Arizona State University  
24 Tempe, AZ  
25

26 4. School of Earth and Space Exploration  
27 Arizona State University  
28 Tempe, AZ  
29  
30  
31  
32

33 Revised version submitted to *Hydrology and Earth System Sciences*  
34 November, 2014  
35  
36  
37  
38  
39  
40  
41

---

42  
43 *Corresponding author address:* Giuseppe Mascaro, School of Sustainable Engineering and the Built Environment,  
44 Arizona State University, ISTB4, Building 75, Room 778b, Tempe, AZ 85287-6004. *E-mail:* gmascaro@asu.edu.

## 1 **Abstract**

2           Future climate projections robustly indicate that the Mediterranean region will experience  
3 a significant decrease of mean annual precipitation and an increase in temperature. These  
4 changes are expected to seriously affect the hydrologic regime, with a limitation of water  
5 availability and an intensification of hydrologic extremes, and to negatively impact local  
6 economies. In this study, we quantify the hydrologic impacts of climate change in the Rio  
7 Mannu basin (RMB), an agricultural watershed of 472.5 km<sup>2</sup> in Sardinia, Italy. To simulate the  
8 wide range of runoff generation mechanisms typical of Mediterranean basins, we adopted a  
9 physically-based, distributed hydrologic model. The high-resolution forcings in reference and  
10 future conditions (30-year records for each period) were provided by four combinations of global  
11 and regional climate models, bias-corrected and downscaled in space and time (from ~25 km, 24  
12 h to 5 km, 1 h) through statistical tools. The analysis of the hydrologic model outputs indicates  
13 that the RMB is expected to be severely impacted by future climate change. The range of  
14 simulations consistently predict: (i) a significant diminution of mean annual runoff at the basin  
15 outlet, mainly due to a decreasing contribution of the runoff generation mechanisms depending  
16 on water available in the soil; (ii) modest variations in mean annual runoff and intensification of  
17 mean annual discharge maxima in flatter sub-basins with clay and loamy soils, likely due to a  
18 higher occurrence of infiltration excess runoff; (iii) reduction of soil water content and actual  
19 evapotranspiration in most areas of the basin; and (iv) a drop in the groundwater table. Results of  
20 this study are useful to support the adoption of adaptive strategies for management and planning  
21 of agricultural activities and water resources in the region.

22  
23 **Keywords:** Climate change, Mediterranean region, distributed hydrologic model, water  
24 resources, statistical downscaling.

## 1 **1. Introduction**

2           Several studies using simulations of future climate robustly indicate the Mediterranean  
3 area as one of the regions of the world to be most severely affected by global changes. This area  
4 has in fact been classified by Giorgi (2006) as a primary hot spot most sensitive to climate  
5 change based on an index that combines variations in precipitation and air temperature from a  
6 multi-model ensemble of climate simulations. Specifically, the majority of climate projections  
7 agree in the prediction of an increase in mean temperature and a reduction in mean precipitation  
8 for the Mediterranean region. For example, climate simulations under the A1B emission scenario  
9 (Nakićević et al., 2000; IPCC, 2007) predict a mean annual warming from 2.2°C to 5.1°C.  
10 Christensen et al. (2008) found that mean annual precipitation is expected to decrease between  
11 4% and 27%. Giorgi and Lionello (2008) provide a good synthesis of several climate simulations  
12 conducted in the Mediterranean region that summarize these main results.

13           Mediterranean watersheds are characterized by high spatial heterogeneity of terrain and  
14 surface properties. These features lead to a hydrologic response that is particularly sensitive to  
15 current climate variability, which is characterized by a strong seasonality and large inter-annual  
16 fluctuations, with alternations of dry and wet periods lasting several years. As a result, these  
17 basins are prone to the occurrence of hydrologic extremes, including drought periods (Hoerling  
18 et al., 2012) and floods and flash-floods (Delrieu et al., 2005; Borga et al., 2007; Silvestro et al.,  
19 2012). Variations in future climate are expected to further impact Mediterranean watersheds at  
20 various spatial and temporal scales (Frei et al., 2006; Beniston et al., 2007; Mariotti et al., 2008),  
21 as also demonstrated through observed data (Mariotti, 2010; Hoerling et al., 2012). This, in turn,  
22 is expected to affect important economic activities, especially those strongly dependent on water  
23 resources such as agriculture and tourism. For example, a future reduction in crop production is

1 anticipated in southern Europe and Mediterranean regions due to decreasing water availability  
2 and degradation of soil and water quality (Olesen and Bindi, 2002; Falloon and Betts, 2010).

3         Given the high sensitivity of Mediterranean basins to climate variability and its  
4 socioeconomic impacts, a multi-institutional research project, named Climate-Induced Changes  
5 on the Hydrology of Mediterranean Basins (CLIMB), was funded by the 7<sup>th</sup> Framework Program  
6 of the European Union (Ludwig et al., 2010). The CLIMB project focused on seven study sites  
7 encompassing different conditions. An approach based on simulations of various climate and  
8 hydrologic models, analysis of environmental and economic data, field campaigns and  
9 stakeholder engagement was adopted to: (i) reduce the uncertainty in the quantification of  
10 climate-induced changes on hydrological responses, and (ii) develop projections and tools to  
11 support planning and management of water resources and associated economic activities.

12         One of the CLIMB sites is the Rio Mannu basin (RMB, 472.5 km<sup>2</sup>) located in an  
13 agricultural area in Sardinia, Italy. This basin has experienced multi-year drought periods (the  
14 most recent during 1990-2000) that resulted in water restrictions for the agricultural and tourist  
15 sectors and led to substantial financial losses. Despite this, no extensive study has been devoted  
16 to evaluating the hydrological vulnerability of this and other Sardinian basins. In this paper, we  
17 provide a contribution to address this issue by quantifying the hydrologic response of the RMB  
18 to different climate change projections. For this aim, four bias-corrected climate forcings are first  
19 set-up for a reference and a future period, using the best-performing combinations of global  
20 (GCM) and regional (RCM) climate models selected by Deidda et al. (2013). These climate  
21 forcings are used as input for the TIN-based Real-time Integrated Basin Simulator (tRIBS)  
22 hydrologic model, which was calibrated and validated with reasonable accuracy as illustrated in  
23 a previous study by Mascaro et al. (2013a). Since climate model outputs are provided at coarse



1 spatial (~25 km) and temporal (daily) scales while the hydrologic model requires hourly data,  
2 proper downscaling tools are applied to increase their spatiotemporal resolution (up to 5 km, 1  
3 h). Hydrologic model outputs under the four climate scenarios, including time series and spatial  
4 maps, are then post-processed to (i) evaluate the impacts on water resources and hydrologic  
5 extremes, and (ii) investigate possible changes on the dominant physical processes in the basin.

6 While the general approach adopted here has been used by other studies (Abbaspour et  
7 al., 2009; Cayan et al., 2010; Liuzzo et al., 2010; Senatore et al., 2011; Montenegro and Ragab,  
8 2012; Sulis et al., 2011, 2012; Camici et al., 2013; Trambly et al., 2013), our methodology has  
9 novel contributions. First, most studies carry out hydrologic simulations at the daily scale. Here,  
10 a process-based model at sub-daily (hourly) resolution is used to simulate the hydrologic  
11 processes typical of Mediterranean basins (Moussa et al., 2007), which are characterized by short  
12 response time and non-linear rainfall-runoff transformation resulting from different runoff  
13 mechanisms (Pinol et al., 1997; Gallart et al., 2002; Beven, 2002). Second, procedures are  
14 applied to downscale bias-corrected climate model outputs to smaller spatial and temporal scales  
15 required for a reliable simulation of the hydrological processes in a medium-sized basin. These  
16 downscaling procedures are then distinct from the bias correction, which instead aims at  
17 correcting the large discrepancy between climate model outputs and observations of precipitation  
18 and temperature in the basin. Finally, the uncertainty associated with different climate models is  
19 taken into account by using four scenarios based on different combinations of GCMs and RCMs.

## 20 21 **2. Study Area**

22 The Rio Mannu di San Sperate at Monastir basin (RMB) is a medium-sized watershed  
23 draining an area of 472.5 km<sup>2</sup>, located in Sardinia, Italy (Fig. 1). It is a representative basin of the  
24 Mediterranean region where the hydrologic response is affected by climate variability, with the

1 occurrence of multi-year drought periods affecting agricultural activities. In this watershed, the  
2 Sardinian Agency for Research in Agriculture (AGRIS) manages an experimental farm of 436  
3 hectares, where hydrometeorological data are collected and productivity of different crops is  
4 monitored. The RMB contributes to the water supply system of Sardinia through a reservoir  
5 located in proximity of the outlet (Fig. 1c). Topography of the RMB is gentle, with a minimum,  
6 mean and maximum elevation of 66, 296 and 963 m.a.s.l. and a mean slope of 17.3%. The  
7 western and central parts of the basin are relatively flat, while a mountain range lies in the  
8 southeastern part. The climate is Mediterranean with a strong seasonality characterized by dry  
9 summers (June to August) and rainfall during the rest of the year having a mean number of rainy  
10 days per month between 6 and 12 days. Precipitation occurs almost always in form of rainfall  
11 with a climatological annual mean of 680 mm. The annual average potential evapotranspiration  
12 is 750 mm (Pulina, 1986). Streamflow is characterized by low flow conditions ( $<1 \text{ m}^3 \text{ s}^{-1}$ )  
13 throughout the year, with a few flood events mostly caused by fall and winter frontal systems  
14 (Chessa et al., 1999; Mascaro et al., 2013b). Land use information from the COoRdination de  
15 l'INformation sur l'Environnement (CORINE) project shows that agriculture (~48%) and sparse  
16 vegetation (~26%) are the dominant categories while other minor classes include olives, forests,  
17 pastures, vineyards and urban areas (Fig. 2a). Soil texture includes mainly six classes: Clay loam  
18 - Clay (37%), Sandy loam - Loam (32%) and Sandy loam - Sandy clay loam (20%) (Fig. 2b).

### 19 20 **3. Data and Methods**

21 The impacts on the hydrologic response due to changes in future climate were quantified  
22 as follows. Outputs of different combinations of GCMs and RCMs were processed to create four  
23 scenarios of hydrometeorological data in a reference (REF) time slice from 1971 to 2000 and a  
24 future (FUT) period from 2041 to 2070. Changes in hydrologic response in terms of availability

1 of water resources and hydrologic extremes were quantified by comparing tRIBS outputs in REF  
2 and FUT periods. Procedures to create the climate forcing for the hydrologic simulations are  
3 discussed in section 3.1, while the main features of the tRIBS model are discussed in section 3.2.

### 4 5 **3.1. Generation of the Climate Forcing**

6 The procedure to create the high-resolution climate forcing in the REF and FUT periods  
7 can be summarized in four steps: (i) selection of GCM-RCM combinations; (ii) large-scale bias  
8 correction of climate model outputs; (iii) disaggregation in space and time of precipitation ( $P$ )  
9 and local-scale bias correction; and (iv) computation of hourly potential evapotranspiration ( $ET_0$ )  
10 from daily minimum ( $T_{min}$ ) and maximum ( $T_{max}$ ) temperature, as illustrated next.

#### 11 12 **3.1.1. Selection of GCM-RCM Combinations**

13 Deidda et al. (2013) evaluated the performance of fourteen combinations resulting from  
14 the coupling of six GCMs with six RCMs from the ENSEMBLES project ([http://ensembles-](http://ensembles-eu.metoffice.com)  
15 [eu.metoffice.com](http://ensembles-eu.metoffice.com)) in some Mediterranean basins, including the RMB. The analysis was  
16 restricted for the future period to the A1B emissions scenario, because (i) this is commonly  
17 considered the most realistic, and (ii) the ENSEMBLES climate models have the most complete  
18 dataset for this scenario. Model outputs at daily resolution in time and  $0.22^\circ$  ( $\sim 25$  km) in space  
19 (see the grid in Fig. 1b) were compared against historical data of daily  $P$  and daily mean,  
20 minimum and maximum temperature ( $T$ ) from the CRU E-OBS dataset (Haylock et al., 2008),  
21 available on the same spatial grid. In the RMB, four combinations of two GCMs and three RCMs  
22 were found by Deidda et al. (2013) to be the most accurate: ECH-RCA, ECH-REM, ECH-RMO  
23 and HCH-RCA (see Table 1 for model descriptions and acronyms). The selection of these GCM-  
24 RCM combinations, hereafter simply referred as selected Climate Models (CMs), also obeys the

1 criterion of having at least two RCMs nested in the same GCM and two different GCMs forcing  
2 the same RCM. The use of four climate scenarios permits characterizing, to a certain extent, the  
3 uncertainties associated with different climate models and possible model combinations.

### 4 5 **3.1.2. Large-scale Bias Correction**

6 Most climate models display some level of deficiencies in reproducing climatological  
7 features and seasonality in large basins (Lucarini et al., 2007; 2008; Hasson et al., 2013; 2014).  
8 In relatively small watersheds, these deficiencies are exacerbated. To reduce these well-known  
9 discrepancies and better reproduce the observed seasonal statistics, a large-scale bias correction  
10 of  $P$  and  $T$  fields predicted by the considered CMs was applied using the E-OBS dataset. For  
11 this, the daily translation method was applied as it has demonstrated skill in prior studies (Wood  
12 et al., 2004; Maurer and Hildago, 2008; Sulis et al., 2012). The method is based on computing  
13 the monthly cumulative distribution functions (CDFs) of observed ( $F_{obs}$ ) and simulated ( $F_{sim}$ )  
14 daily variables. For a given daily output variable of a climate model,  $x$ , the unbiased value,  $x^*$ , is  
15 obtained as  $x^* = F_{obs}^{-1}[F_{sim}(x)]$ , where  $F_{obs}^{-1}$  is the inverse of  $F_{obs}$ . To reproduce the seasonal  
16 cycles,  $F_{obs}$  and  $F_{sim}$  functions were derived on a monthly basis, i.e. pooling together all daily  
17 observations (or simulated records) for each month. The procedure was applied to the daily  $P$   
18 and the daily mean, minimum and maximum  $T$ . In this effort,  $T$  was also corrected to account for  
19 the different elevations adopted by CMs and E-OBS via a spatial and dynamic lapse rate.

### 20 21 **3.1.3. Precipitation Downscaling and Local-scale Bias Correction**

22 One source of uncertainty of climate models is related to the smoothing effect induced by  
23 their coarse spatial ( $\sim 25$  km) and temporal (24 h) resolution (Wilby and Wigley, 1997; Maraun et  
24 al., 2010; Bardossy and Pegram, 2011). This is especially true for  $P$ , which is characterized by

1 high intermittency and strong fluctuations in space and time, also affected by local orographic  
2 effects. To reproduce this feature, we used the precipitation downscaling technique based on a  
3 multifractal model (Space-Time Rainfall, STRAIN) that is able to recreate the scale invariance  
4 and multifractal properties of precipitation fields observed from coarse to small spatiotemporal  
5 scales (Deidda et al., 1999, 2000). This is achieved by means of a stochastic generator of  
6 multiplicative multifractal cascades, whose parameters can be derived from the large-scale  
7 rainfall amount,  $R$  ( $\text{mm h}^{-1}$ ), according to empirical calibration relations.

8 For the RMB, Mascaro et al. (2013a) calibrated the algorithm with rainfall observations  
9 at 1-min resolution of 204 gages, collected in the period 1986-1996 in the coarse spatial domain  
10 of  $104 \times 104 \text{ km}^2$  shown in Fig. 1b. A total of 800 precipitation events were used to estimate the  
11 model parameters and identify the calibration relations as a function of  $R$  for our study area. As  
12 described in detail in Mascaro et al. (2013a), two tests were conducted to validate the  
13 downscaling method. First, the model capability to capture the small-scale rainfall distribution  
14 within the coarse-scale domain was evaluated by visually comparing observed and synthetic  
15 empirical cumulative distribution functions for each rainfall event. An example of this  
16 comparison is provided in Mascaro et al. (2013a; Fig 6), which shows relatively good skill of the  
17 downscaling routine. A second validation was carried out specifically on the study basin, by  
18 comparing observed and simulated daily mean areal precipitation (MAP) from 1925 to 1935. In  
19 this period, discharge data are available to calibrate and validate the hydrologic model (see  
20 section 3.2) and rainfall observations were only collected at daily resolution. For each rainy day,  
21 the downscaling model was applied from the coarse to the fine resolution generating an ensemble  
22 of 50 disaggregated fields. The observed daily MAP in the basin was calculated by applying  
23 Thiessen polygons to the observations of 13 available gages, and the simulated MAP was

1 derived by aggregating the synthetic grids at daily resolution and computing the spatial basin  
2 average. The Root Mean Square Error (RMSE) and bias between the observed MAP and the  
3 ensemble average from the downscaling model were then calculated. As reported in Mascaro et  
4 al. (2013a; Table 7), the RMSE has little interannual variability (average value of 4.38 mm),  
5 while the bias is negative (mean of  $-0.89$  mm), indicating that the downscaling procedure tends  
6 to slightly underestimate the observed MAP (less than 10 %).

7 In this study, the downscaling routine was applied by: (i) aggregating the bias-corrected  
8 daily  $P$  outputs of the CMs in the coarse spatial domain to compute  $R$ , (ii) using the RMB  
9 calibration relations to derive parameters conditioned on  $R$ , and (iii) applying STRAIN to  
10 downscale  $R$  to 5-km and 1-h resolution. The disaggregated fields were also corrected for  
11 orographic effects using the elevation modulation function described by Badas et al. (2006). In  
12 principle, the statistically-based disaggregation technique requires the generation of an ensemble  
13 of  $P$  downscaled fields, each representing an equally-probable realization of the coarse condition.  
14 For example, Mascaro et al. (2013a) generated an ensemble of 50  $P$  downscaled members to  
15 calibrate and validate the tRIBS model. In this study, we only created a single disaggregated  
16 realization for each selected CM for two main reasons. First, climate models do not reproduce  
17 weather evolution in time according to deterministic rules, but rather reproduce the statistical  
18 peculiarity of the climatic features (Lucarini, 2008). In other words, a one-to-one correspondence  
19 between an observation and a climate model simulation does not exist for a certain day. Second,  
20 the multi-decadal length of the REF and FUT periods (30 years) is large enough to assure that  
21 the use of a single disaggregated member is able to capture a large portion of the small-scale  
22 rainfall variability occurring within each time slice.

1           After the disaggregation, a last procedure for local-scale bias correction of  $P$  was applied  
2 to correct residual biases mainly due to the coarseness of the rain gage network used for the E-  
3 OBS dataset (Haylock et al., 2008), which may fail to reproduce the local features of  $P$  fields.  
4 The procedure is illustrated in Fig. 3. The climatological monthly average of the mean areal  
5 precipitation (MAP) in the RMB was first calculated using data observed by 13 gages within the  
6 catchment over the period 1951-2008. In parallel, the same variable was computed for the  
7 disaggregated fields from all selected CMs in the same period. The ratio between observed and  
8 simulated mean monthly MAP was then used as a correction on the downscaled  $P$  fields to  
9 eliminate the residual bias.

#### 10 11 **3.1.4. Computation of Potential Evapotranspiration**

12           For each CM, we estimated the gridded  $ET_0$  at hourly resolution starting from the bias-  
13 corrected daily  $T_{min}$  and  $T_{max}$ . For this purpose, the  $T$  fields at  $\sim 25$ -km resolution were first  
14 interpolated in the same 5-km grid used for  $P$  as in Liston and Elder (2006), and then corrected  
15 for elevation variations of the 5-km grid using a dynamic lapse rate. Then, the downscaling  
16 technique proposed by Mascaro et al. (2013a) was applied to derive the maps of hourly  $ET_0$  from  
17  $T_{min}$  and  $T_{max}$ . The method requires an estimate of the daily  $ET_0$  by applying the Hargreaves  
18 formula with  $T_{min}$  and  $T_{max}$  and a linear correction to derive the value returned by the Penman-  
19 Monteith equation. Next, dimensionless functions that reproduce, for each month, the sub-daily  
20 variability of  $ET_0$  are used to derive the hourly  $ET_0$  from the daily estimate. The procedure was  
21 calibrated and tested in the RMB using meteorological data (required to apply the Penman-  
22 Monteith formula) observed in one station over 1995-2010. To validate the method, we  
23 calculated the RMSE and bias between (i) the hourly  $ET_0$  computed using the Penman-Monteith  
24 formula, (ii) the hourly  $ET_0$  obtained with the disaggregation method starting from  $T_{min}$  and  $T_{min}$ .

1 Results show that, despite the downscaling procedure slightly underestimates the hourly  $ET_0$   
2 (negative mean bias of  $-0.010 \text{ mm h}^{-1}$ ), performances are overall fairly good, as indicated by the  
3 low RMSE (mean of  $0.030 \text{ mm h}^{-1}$ ). More details are provided by Mascaro et al. (2013a).

### 4 5 **3.2. The Hydrologic Model**

6 tRIBS is a physically-based, distributed hydrologic model that is able to continuously  
7 simulate the coupled water and energy balance (Ivanov et al., 2004a,b). Terrain is represented  
8 through Triangulated Irregular Networks (TINs) used to discretize the domain into Voronoi  
9 polygons. The use of TINs allows for computational savings as compared to grid-based models  
10 due to the multi-resolution domain representation (Vivoni et al., 2004; 2005). This feature is  
11 crucial for the feasibility of multi-decadal hydrologic simulations carried out in climate change  
12 studies. The spatially-distributed hydrologic response is reproduced by solving equations of the  
13 water and energy fluxes in each Voronoi polygon. In tRIBS, several hydrologic processes are  
14 represented, including canopy interception, infiltration and soil moisture redistribution, lateral  
15 water movement in the unsaturated and saturated zones, evaporation from bare soil and wet  
16 canopies, plant transpiration, overland flow in the hillslopes, and routing in the stream channel.  
17 The infiltration scheme allows for several configurations of soil moisture in the unsaturated and  
18 saturated zones. As a result, runoff generation is possible via four mechanisms: saturation excess,  
19 occurring when the single domain element is fully saturated from below; infiltration excess,  
20 occurring when the element is saturated from above by a high-intensity rainfall; perched return  
21 flow, occurring as lateral flow on the surface of a cell from a saturated layer in an upslope  
22 element; and groundwater exfiltration, occurring as lateral redistribution in the phreatic aquifer.  
23 As a result, this model has the capability to represent the strongly non-linear rainfall-runoff



1 relation typical of Mediterranean basins. The specific treatment of each process is described in  
2 detail by Ivanov et al. (2004a).

3 Model equations are parameterized through lookup tables and related spatial maps of soil  
4 texture and land cover. Precipitation can be provided as point time series or spatial grids. This  
5 last alternative is used in this study to force the model with gridded downscaled fields, as  
6 described in section 3.1.3. Computing actual evapotranspiration ( $ET_a$ ) and its components  
7 requires estimating  $ET_0$ . This can be performed by applying the Penman-Monteith equation with  
8 meteorological data or by forcing the model with  $ET_0$  computed off-line, either in point or grid  
9 format. Again, this last alternative is used in this study to provide downscaled  $ET_0$  as described  
10 in section 3.1.4.  $ET_a$  is then estimated as a fraction of  $ET_0$  based on the available soil moisture  
11 using a piecewise-linear equation (Mahfouf and Noilhan, 1991; Ivanov et al., 2004a). Model  
12 outputs include time series of discharge at any location in the stream network and spatial maps of  
13 hydrologic state variables and fluxes (e.g., evapotranspiration, soil water content at different  
14 depths, ground water table position) at specified times or integrated over defined periods.

15 The model has been previously used in the areas of hydrometeorology (Mascaro et al.,  
16 2010; Moreno et al., 2013), climate change (Liuzzo et al., 2010) and ecohydrology (Mahmood  
17 and Vivoni, 2014). Recently, Mascaro et al. (2013a) calibrated and validated tRIBS in the RMB  
18 against streamflow data. A TIN with 171,078 nodes was derived from a 10-m Digital Elevation  
19 Model (DEM), retaining 3.6% of the DEM nodes and resulting in a vertical accuracy of 3 m.  
20 Vegetation parameters, involved in the processes of rainfall interception and estimation of  $ET_a$ ,  
21 have been derived for the land cover classes of Fig. 2a, based on values published in literature  
22 for similar land cover classes. The model was calibrated for one year (1930) and validated for  
23 two years (1931-1932), where daily discharge data collected by the Italian Hydrologic Survey

1 were judged to have the highest quality. To identify robust model parameters while using a  
2 relatively short record of observations, we selected a wet year (total annual runoff of 183 mm)  
3 with several flood events for calibration and two dry years (annual runoff of 76 and 71 mm) with  
4 a few floods for validation. Since in the period 1930-1932 hydrometeorological data include  
5 rainfall data at daily resolution and daily  $T_{min}$  and  $T_{max}$ , the downscaling procedures previously  
6 illustrated were used to create the high-resolution forcings. Despite the presence of several  
7 uncertainty sources, Mascaro et al. (2013a) showed adequate performances in the RMB for the  
8 tRIBS model, which is used here with the same parameterization.

## 9 10 **4. Results and Discussion**

11 In this section, we first analyze the monthly variability of the basin-averaged  $P$  and  $T$   
12 fields with the goal of highlighting the main climatological differences between the REF and  
13 FUT periods. Subsequently, we present results of the hydrologic simulations forced with the  
14 disaggregated  $P$  and  $ET_0$ . Specifically, the changes on stream discharge ( $Q$ ) are evaluated,  
15 focusing on both water resources availability and hydrologic extremes. Finally, variations in  
16 evapotranspiration ( $ET_a$ ), soil water content ( $SWC$ ), and ground water level are explored.

### 17 18 **4.1. Changes in Climate Forcing**

19 Fig. 4 reports different features of mean monthly variability of basin-averaged  $P$  grids for  
20 the four CMs in the REF and FUT periods: mean areal precipitation (MAP; Figs. 4a,b), number  
21 of rainy days ( $N$ ; Fig. 4c,d), and mean precipitation intensity in rainy days ( $I$ ; Figs. 4e,f). In the  
22 left panels, the bars represent the mean  $\pm$  standard deviation across the four CMs of the 30-year  
23 monthly average of each variable. Note that the months are ordered according to the water year.

1 For each CM, the relative monthly changes  $\Delta\alpha$  (%) from REF to FUT, computed by the  
2 following eq. (1) for a generic variable  $\alpha$ , are plotted in the right panels:

$$3 \quad \Delta\alpha = \frac{\alpha_{FUT} - \alpha_{REF}}{\alpha_{REF}} \cdot 100, \quad (1)$$

4 where  $\alpha_{FUT}$  and  $\alpha_{REF}$  are the 30-year monthly mean of  $\alpha$  in FUT and REF, respectively. Eq. (1)  
5 is used in this paper for all variables, except for  $T$  for which the changes are calculated through  
6 the simple difference between FUT and REF.

7 Fig. 4a shows that mean areal precipitation (MAP) is expected to decrease in FUT in all  
8 months, except in winter (December to February) where mean values are similar. Negative  
9  $\Delta$ MAP are predicted by all combinations in September, November, March, April, and May,  
10 while in the other months the sign and magnitude of  $\Delta$ MAP vary among the four combinations,  
11 even significantly (e.g., October and December), suggesting higher uncertainty in climate  
12 predictions (Fig. 4b). The mean annual MAP in REF and FUT periods and the relative changes  
13 are reported in Table 2 for each combination: we can observe that the four CMs predict a  
14 decrease in annual precipitation from -7% (ECH-REM) to -21% (HCH-RCA). These results are  
15 consistent with a number of studies that analyzed climate projections in the Mediterranean region  
16 under the A1B scenario (e.g., IPCC, 2007; Giorgi and Lionello, 2008; Senatore et al., 2011).

17 Similarly to MAP, the number of rainy days ( $N$ ) is expected to decrease in FUT over the  
18 year except for winter, where no significant variations are expected (Fig. 4c). Changes in  $N$  are  
19 similar for the four CMs, indicating lower model uncertainty in predicting rainfall occurrence  
20 (Fig. 4d). The projections for the mean precipitation intensity ( $I$ ) are instead characterized by  
21 high variability over the year and across the combinations. Fig. 4e shows that higher  $I$  is  
22 predicted in FUT during the months with larger total precipitation (from October to December),  
23 and most of the summer (June and July). The rainfall intensity in FUT will be lower from

1 January to May and in August and September. Fig. 4f shows that sign and magnitude of  $\Delta I$  are  
2 different in each month, highlighting a large uncertainty across the CMs. Since rainfall intensity  
3 is a crucial variable influencing runoff, this underlines the importance of using multiple  
4 combinations of GCMs and RCMs to account for climate model uncertainty in simulating  
5 hydrologic responses.

6 The mean monthly  $T$  in REF and FUT periods is reported in Fig. 5a, while the relative  
7 changes ( $\Delta T$ ) are shown in Fig. 5b. As found in previous works (e.g., Giorgi and Lionello, 2008),  
8 the uncertainty in the prediction of future  $T$  is considerably reduced as compared to  $P$ . All  
9 scenarios show a future increase of  $T$  for all months with a low standard deviation among the  
10 combinations. Higher  $\Delta T$  are expected in summer, with an average yearly variation from 1.87°C  
11 (ECH-RCA) to 3.08°C (HCH-RCA), see Table 2 for more details. As for  $P$ , the HCH-RCA  
12 combination predicts the largest variations in  $T$ . Overall, the monthly changes in  $P$  and  $T$   
13 predicted by the CMs are very similar to the forcing used in another Mediterranean climate  
14 change study carried out by Senatore et al. (2011) in a watershed in southern Italy.

#### 15 16 **4.2. Changes in Stream Discharge and Runoff Mechanisms**

17 The hourly gridded  $P$  and  $ET_0$  from the four selected CMs were used to force the tRIBS  
18 model. A spin-up interval of two years was adopted before each 30-year run, totaling 256 years  
19 of simulation. This computational effort was carried out using the parallelized version of tRIBS  
20 (Vivoni et al., 2011), which took 880 hours of CPU time over 64 processors. Model outputs  
21 including time series at distributed locations and spatial maps of hydrologic fluxes and state  
22 variables were post-processed to quantify the changes from REF to FUT periods. Fig. 6 presents  
23 results for the mean monthly  $Q$  at the RMB outlet, according to Eq. (1). Despite no significant  
24 variation in MAP is anticipated during winter,  $Q$  is predicted to diminish in FUT for all months

1 (Fig. 6a) and by all scenarios (Fig. 6b). A slightly positive  $\Delta Q$  is only found in December and  
2 June in one of the combinations. Note that the decrease of  $Q$  in months with little variation in  $P$   
3 can be mostly ascribed to the diminution of the runoff portion due to groundwater exfiltration  
4 occurring throughout the year, as better illustrated below. Table 2 shows the mean annual  
5 changes, which range from -17% (ECH-REM) to -50% (HCH-RCA). Note that the different  
6 percentages observed for each CM are related to the decrease in  $P$ .

7         The change in mean annual  $Q$  was further analyzed using the streamflow time series for  
8 the 20 sub-basins shown in Fig. 2b (sub-basin 20 refers to the entire RMB). The terrain, soil  
9 texture and land cover characteristics of the sub-basins are summarized in Table 3. The relation  
10 between  $\Delta Q$  and the contributing area ( $A_c$ ) is shown in Fig. 7a, in terms of mean and standard  
11 deviation across the CMs. Results indicate the presence of two groups of sub-basins. The first  
12 includes five sub-watersheds labeled as 1-4 and 9, with a slightly positive mean  $\Delta Q$  ( $\sim+8\%$ ) and  
13 higher standard deviation that suggests larger uncertainty due to the different climate forcings.  
14 These sub-basins are located in the northwestern portion of the RMB and are characterized by  
15 relatively low slope (mean of  $\sim 8\%$ ) and dominance of Clay loam – Clay soil texture ( $> 77\%$ ) and  
16 Agriculture land use ( $> 71\%$ ). The second group includes all the other sub-basins and displays a  
17 significant drop of  $Q$  (average of about -28%) and lower variability across the CMs.

18         To investigate the physical reasons underlying the changes in  $Q$ , we inspected the  
19 variation in the dominant runoff mechanisms. The partitioning of  $Q$  at the RMB outlet into  
20 infiltration and saturation excess ( $Q_{IE}$  and  $Q_{SE}$ ), groundwater exfiltration ( $Q_{GE}$ ) and perched  
21 return flow ( $Q_{PR}$ ) runoff is shown for each CM forcing in Fig. 8a for the REF period. The four  
22 combinations indicate the dominance of  $Q_{GE}$ , followed by  $Q_{SE}$ ,  $Q_{IE}$  and  $Q_{PR}$ . Fig. 8b presents the  
23 change in the amount of total  $Q$  produced for each mechanism. All CMs predict a decrease in

1  $Q_{SE}$ ,  $Q_{GE}$ ,  $Q_{PR}$ , which are the components controlled by water availability in the soil, while  $Q_{IE}$  is  
2 expected to grow for all combinations except for ECH-RCA. This last runoff type occurs when  
3 the rainfall rate exceeds the infiltration capacity, suggesting that a variation of  $Q_{IE}$  in FUT may  
4 be due to a change in rainfall intensities during extreme events. To analyze this hypothesis, we  
5 derived the mean of the annual maxima of hourly  $P$  over the 30-year records in FUT and REF  
6 periods for each CM. Next, we computed the variation between these two average  $P$  maxima  
7 from REF to FUT and we found a perfect correlation with the changes in  $Q_{IE}$ .

8         Modifications in runoff generation mechanisms within the basin were evaluated by  
9 focusing on the sub-basins. We first point out that the mean annual change in  $P$  is expected to be  
10 fairly constant in all sub-basins (not shown), suggesting that spatial differences may be mostly  
11 ascribed to surface and subsurface properties. In sub-basins 1-4 and 9 located in the northwest  
12 part of the RMB,  $Q_{SE}$ ,  $Q_{GE}$ ,  $Q_{PR}$  decrease considerably more than the rest of the watershed (mean  
13 changes of -75%, -70% and -50%), while  $Q_{IE}$  slightly grows (mean change of +10%). For this set  
14 of sub-basins, we can conclude that: (i) the small increase in  $Q$  is due to a growth in  $Q_{IE}$ ; (ii)  
15 higher occurrence of  $Q_{IE}$  is due to more impermeable soils that make these sub-basins more  
16 sensitive to changes in rainfall intensity; and (iii) higher occurrence of  $Q_{IE}$  and the reduced buffer  
17 effect due to a deeper groundwater table (mean values shown in Fig. 7b for the FUT case) make  
18 their runoff response more uncertain for the CMs. For the other set of sub-basins: (i) total  $Q$   
19 decreases due to a general reduction of all components; and (ii) the uncertainty in runoff  
20 response is relatively lower, especially for increasing  $A_c$ .

### 21 22 **4.3. Changes in Hydrologic Extremes**

23         Changes in hydrologic extremes are investigated in terms of (i) low flow persistence,  
24 which can be assumed as a proxy of drought periods, and (ii) occurrence of high flows. To

1 analyze the impacts on the first type of extremes, we computed Flow Duration Curves (FDCs)  
2 for  $Q$  at the outlet. Fig. 9 clearly shows a downward shift in the FDCs over most exceedances,  
3 consistent with the predicted reduction of total  $Q$  in the FUT period. To identify the low flow  
4 conditions, we first calculated a threshold discharge,  $Q_{LF}$ , as the streamflow corresponding to the  
5 70% percentage of exceedance for the REF period (circle in Fig. 9). Low flow conditions were  
6 then defined as the periods during which  $Q < Q_{LF}$ . Fig. 10a shows that the monthly mean number  
7 of low flow days is expected to increase in FUT for about 5 days for each month, implying more  
8 frequent dry conditions. The annual average of the maximum consecutive length of low flow  
9 days is reported in Fig. 10b. In current conditions, all combinations robustly simulate a value of  
10 about 50 days occurring during the summer months. In the future, the length is expected to  
11 increase from 19 to 52 days on average, depending on the CM, thus extending the low flow  
12 conditions to spring and/or fall. This result confirms and further details previous findings on  
13 future drought in the Mediterranean region (e.g., Beniston et al., 2007).

14 Concerning the second type of extremes, we used the time series of  $Q$  at the outlet and 19  
15 internal sub-basins. For the REF and FUT periods: (i) the index-flood was obtained for each sub-  
16 basin by averaging the corresponding 30 yearly  $Q$  maxima, and (ii) the ratio between the index-  
17 flood and the corresponding  $A_c$  was computed. This ratio, labeled as  $\mu_c$ , was found to remain  
18 fairly constant as a function of  $A_c$  and, thus, was used to remove the effect of their size. We then  
19 computed the changes  $\Delta\mu_c$  from REF to FUT and explored their relation with terrain attributes  
20 and soil texture. Results of this analysis are summarized in Fig. 11 where  $\Delta\mu_c$  is plotted against  
21 the mean sub-basin slope for each CM. Predictions under three combinations (ECH-REM, ECH-  
22 RMO and HCH-RCA) indicate that the magnitude of the mean annual  $Q$  maxima will increase in  
23 the FUT period as the basin slope decreases and when soils are dominated by clay and loam (Fig.

1 11b, c, and d). For the ECH-RCA case, a negative  $\Delta\mu_c$  was instead systematically detected for all  
2 sub-basin, without any clear link to soil type and basin slope (Fig. 11a). This behavior is again  
3 explained with changes in the rainfall intensities of extreme events: for the first three CMs, the  
4 mean of the annual maxima of hourly  $P$  is expected to increase in the future, while a reduction is  
5 predicted for the latter CM. As previously discussed, this is reflected in similar changes in  $Q_{IE}$ ,  
6 which is the dominant runoff mechanism during floods. It is worth noticing that the highest  
7 positive  $\Delta\mu_c$  in Figs. 11b-d are found for sub-basins 1-4 and 9, characterized by lower slope and  
8 dominated by more impermeable soils (clay and loam), where a relatively higher increase in  $Q_{IE}$   
9 is expected.

10

#### 11 **4.4. Changes in Evapotranspiration and Soil Water Content**

12 Fig. 12a shows time series of the mean and standard deviation of monthly average  $ET_\theta$   
13 and  $ET_a$  in the REF and FUT periods. As expected, projections of higher  $T$  in the future leads to  
14 increasing  $ET_\theta$ . In contrast, a reduced  $ET_a$  is simulated for most of the year, except for January,  
15 May and November. This is mainly due to the reduction of soil water content ( $SWC$ ) in the root  
16 zone in the FUT period, which is related to the decreases of  $P$ . This is clearly shown by Fig. 12b,  
17 where we can observe a marked reduction throughout the year of  $SWC$  and a negative change of  
18  $ET_a$ , despite a systematic positive variation of  $ET_\theta$ . These findings are mostly in accordance with  
19 Senatore et al. (2011) who found decreasing  $ET_a$  in winter and diminishing  $SWC$  across the year.

20 The feedbacks among changes in  $ET_a$  and  $SWC$ , and their relation with meteorological  
21 forcing ( $P$  and  $T$ , and consequently  $ET_\theta$ ) and basin characteristics (soil texture and topography)  
22 were investigated using the spatial model outputs. As an example, Figs. 13 and 14 show maps of  
23  $\Delta P$ ,  $\Delta SWC$ ,  $\Delta ET_\theta$  and  $\Delta ET_a$  in winter (December-February) and spring (March-May) seasons,  
24 which are characterized by the smallest and largest  $\Delta P$  and  $\Delta ET_\theta$  in the ECH-RCA forcing. The



1 behavior found in the other seasons is similar to the dynamics in spring, while results derived for  
2 other climate model combinations are not significantly different.

3 In winter, the basin-averaged changes in  $P$  are small ( $\Delta P = -1.92\%$ ), limiting  $SWC$   
4 decreases and leaving enough soil water for evapotranspiration. A higher  $ET_0$  ( $\Delta ET_0 = +3.30\%$ )  
5 allows  $ET_a$  to rise slightly ( $\Delta ET_a = +0.14\%$ ). The combined effect of decreasing water input  
6 from  $P$  and higher  $ET_a$  causes a basin-averaged reduction of  $SWC$  of  $-3.66\%$ . The pattern of  
7  $\Delta SWC$  (Fig. 13b) is mostly influenced by soil texture and, to a less extent, by  $\Delta P$  (Fig. 13a) and  
8  $\Delta ET_0$  (Fig. 13c). Lower  $\Delta SWC$  (from  $-2.0\%$  to  $+0.9\%$ ) are found in the Sandy loam – Loam class  
9 where  $\Delta P$  is slightly negative to positive (indicated with L in Fig. 13b). In these regions, soil  
10 water is available to be extracted at a higher rate ( $\Delta ET_0$  varies from  $+3.1\%$  to  $+4.0\%$ ), thus  
11 causing  $ET_a$  to grow from  $+3\%$  to  $+8\%$ .  $SWC$  is expected to decrease more significantly (from  $-$   
12  $3\%$  to  $-20\%$ ) in areas of Clay loam – Clay and Sandy loam – Sandy clay loam (labeled H in Fig.  
13 13b), where  $P$  decreases by up to  $-7\%$  and  $ET_0$  does not vary substantially ( $+2\%$ ). Note that this  
14 area mostly contains sub-basins 1-4, and 9 that experience the highest reductions of  $Q_{SE}$ ,  $Q_{GE}$  and  
15  $Q_{PR}$ . As expected, the spatial pattern of  $\Delta ET_a$  is highly correlated with  $\Delta SWC$  (correlation  
16 coefficient of 0.80), with a minor dependence on  $\Delta ET_0$ , although its signature is also apparent.

17 In spring,  $P$  is predicted in FUT to be noticeably lower (basin-averaged  $\Delta P = -28.37\%$ )  
18 and  $ET_0$  higher ( $\Delta ET_0 = +5.51\%$ ). As a consequence, the decrease in  $SWC$  is more significant  
19 ( $\Delta SWC = -7.13\%$ ) and the water available for evapotranspiration is limited, causing  $ET_a$  to  
20 diminish ( $\Delta ET_a = -2.12\%$ ), despite the positive trend of  $ET_0$ . In most of the basin,  $\Delta SWC$  ranges  
21 from  $-6\%$  to  $-7\%$  (L areas in Fig. 14b), likely due to the relatively low spatial variability of  $\Delta P$   
22 (Fig. 14a). Higher drops in  $SWC$  (up to  $-20\%$ ) occur in the areas dominated by Sandy loam –  
23 Sandy clay loam where  $P$  decreases more (H areas in Fig. 14b). Topography also plays a role, as

1 reduced drops of  $SWC$  appear in areas of flow convergence close to streams.  $\Delta ET_a$  (Fig. 14d) is  
2 still well correlated to  $\Delta SWC$  (correlation coefficient of 0.75) and also affected by  $\Delta ET_0$  (Fig.  
3 14c).  $ET_a$  remains essentially constant in the areas labeled with L in Fig. 14d, characterized by  
4 lower changes in  $SWC$  and relatively higher  $\Delta ET_0$ .  $ET_a$  decreases instead significantly (up to -  
5 12%; H areas) in the regions where the drop of  $SWC$  is the largest and changes in  $ET_0$  are  
6 modest. The effect of topography can be better appreciated in the map of  $\Delta ET_a$ : higher values  
7 (+10%) are simulated in the areas close to the stream network with higher availability of water.

8 This analysis reveals that, despite higher  $ET_0$ , the RMB will experience in the future a  
9 decrease in  $ET_a$  in most areas and times of the year, due to the lack of soil water caused by lower  
10 rainfall. The only season with a different behavior is winter, where  $P$  is expected to decrease to a  
11 lesser extent or slightly increase, thus limiting the reduction in  $SWC$  and leading in certain areas  
12 to higher  $ET_a$ . The patterns of  $SWC$  and  $ET_a$  are mainly controlled by soil texture and the  
13 interaction of  $P$  and  $ET_0$ . Terrain plays also a role when reductions of  $P$  are more significant.

#### 14 15 **4.5. Changes in Groundwater**

16 A last analysis was devoted to evaluate the impact of climate change on groundwater. For  
17 this aim, we computed the difference between the basin averaged groundwater level at the end of  
18 the 30-year simulation in FUT and REF periods. For all sets of climate forcing, we found a drop  
19 of the water table ranging from 1.0 to 4.6 meters, constant across the year. The amount of the  
20 drop simulated for each CM is linked to the corresponding diminution in  $P$  input (lowest for  
21 ECH-REM and highest for HCH-RCA). In fact, a decreasing rainfall input leads to a decrease of  
22 the soil water content in the unsaturated zone and reduces the recharge to the aquifer. This result  
23 is confirmed by the diminishing occurrence of  $Q_{GE}$  (Fig. 8b).

24

## 1 **5. Conclusions**

2 In this study, we quantified the impacts of climate change on water resources and  
3 hydrologic extremes in an agricultural Mediterranean basin of 472.5 km<sup>2</sup> located in Sardinia,  
4 Italy. For this aim, the process-based tRIBS model was used to capture the large variety of the  
5 hydrologic conditions occurring in Mediterranean areas. The forcings in reference (1971-2000)  
6 and future (2041-2070) period were provided by outputs from four combinations of GCMs and  
7 RCMs, bias-corrected and downscaled in space and time through statistical tools. The adoption  
8 of disaggregation tools was crucial to create high-resolution (5-km, 1-h) inputs required to apply  
9 this type of hydrologic model. Outputs of the hydrologic simulations were then compared in the  
10 reference and future periods to quantify the changes in several variables. The main results of this  
11 study are summarized below.

12 At annual scale, all CMs predict decreasing  $P$  (mean of -12.70%) and increasing  $T$  (mean  
13 +2.18°C), leading to a significant diminution of  $Q$  (-32.55%) at the basin outlet. The changes in  
14 future climate will mostly lead to a reduction of those runoff generation mechanisms that depend  
15 on water available in the soil, namely  $Q_{SE}$ ,  $Q_{PR}$  and  $Q_{GE}$ . A higher degree of uncertainty across  
16 the climate model combinations was found while predicting the variation in  $Q_{IE}$ , which depends  
17 on the combined effect of rainfall intensities and soil hydraulic properties.

18 Changes in annual  $Q$  were also investigated at distributed locations, finding two sets of  
19 sub-basins with different behavior. In the northwest region, characterized by flatter terrain and  
20 clay-loam soils, the mean  $Q$  is expected to increase somewhat in the future. Specifically, a small  
21 growth in  $Q_{IE}$  is anticipated, while  $Q_{SE}$ ,  $Q_{PR}$  and  $Q_{GE}$  will have the largest reduction over the  
22 basin. Hydrologic responses in this area under different CMs are affected by higher uncertainty,  
23 due to the higher occurrence of the faster runoff component ( $Q_{IE}$ ) and the lower contribution of

1 slower subsurface components ( $Q_{PR}$  and  $Q_{GE}$ ) that tend to attenuate the variability of the climate  
2 forcing. In contrast, for other sub-basins in the RMB,  $Q$  is anticipated to diminish with relatively  
3 low uncertainty across the four CMs, due to a decreasing contribution of all runoff components.

4 At basin scale, the combined effect of lower  $P$  and higher  $T$  leads to increasing  $ET_0$  and  
5 decreasing  $SWC$  throughout the year, and diminishing  $ET_a$  over all months except for winter. The  
6 spatiotemporal analysis of the interactions between  $SWC$  and  $ET_a$  reveals that: (i) in most areas  
7 and times of the year, negative changes of  $P$  lead to a reduction in  $ET_a$ , because there is not  
8 enough soil water to sustain the higher evaporative demand; (ii) in winter, some areas experience  
9 a modest decrease or a slight rise of  $P$ , leading to local growth in  $ET_a$ ; (iii) soil texture controls  
10 the amount of the variations in  $SWC$ , with higher drops in the Sandy loam – Sandy clay loam  
11 class; and (iv) topography also plays a role with positive changes in  $SWC$  and  $ET_a$  found in areas  
12 of flow convergence near the stream network.

13 To our knowledge, this is the first climate change study conducted in Sardinia at the  
14 watershed scale. Results suggest that the basin hydrologic regime will be significantly impacted  
15 by variations in future climate. The diminution in annual  $Q$  at the outlet implies that: (i) the  
16 inflow at the reservoir located in proximity of the outlet will be reduced, and (ii) more frequent  
17 and longer low flow conditions, which are an indication of hydrological drought, are expected. In  
18 addition, agricultural areas are anticipated to experience the largest drop in  $SWC$  in the root zone  
19 (mean of -6%) among all land cover classes. This finding, in conjunction with the decreasing  $P$ ,  
20 may have important impacts on the crops (especially the rainfed areas) that are currently grown  
21 in the basin. As a result, the implications of this study are useful to support the selection of  
22 adaptive strategies for water and crop management and planning under climate change, as well  
23 as to quantify the social and economic vulnerability of the region.

1           Finally, we point out that, as any climate change study, the methodology adopted here is  
2 affected by uncertainties and limitations. The climate model uncertainty was addressed by  
3 selecting the best performing four combinations of global and regional climate models in  
4 reproducing precipitation and temperature in the study basin. Due to the lack of observations (a  
5 common problem in this region), the hydrologic model was calibrated and validated only with  
6 three years of data. To address this issue and identify robust model parameters, we selected the  
7 calibration and validation periods characterized by markedly different hydrologic conditions. A  
8 single set of techniques, commonly used in climate change studies, was applied to correct the  
9 bias of CM outputs. In addition, statistical downscaling tools were adopted to simulate the small-  
10 scale variability of precipitation and temperature, with calibration relations assumed stationary  
11 from current to future climate. While a process-based model like tRIBS has the potential to  
12 capture the basin response at high-resolution and allows conducting distributed analyses, current  
13 computational constraints have limited the possibility to deal with other sources of uncertainty,  
14 including testing the effect of different types of bias correction methods (e.g., Trambly et al.,  
15 2013). Finally, we plan to devote future work to address the uncertainty of hydrologic modeling,  
16 by comparing outputs from different models applied in the RMB by several research groups in  
17 the context of the CLIMB project.

## 18 19 **Acknowledgements**

20           This study was developed as part of the project CLIMB (<http://www.climb-fp7.eu>)  
21 funded by the European Commission's 7th Framework Program. The authors also thank financial  
22 support by the Sardinian Region L.R. 7/2007, funding call 2008. They acknowledge the  
23 ENSEMBLES project, funded by the EU-FP6 through contract GOCE-CT-2003-505539, and the  
24 data providers in the ECA&D project for making RCMs outputs and the E-OBS data set

- 1 available. Two anonymous reviewers are thanked for their comments that helped to improve the
- 2 quality of the manuscript.

## 1 **References**

- 2 Abbaspour, K. C., Faramarzi, M., Ghasemi, S. S., and Yang, H.: Assessing the impact of climate  
3 change on water resources in Iran, *Water Resour. Res.*, 45, W10434,  
4 doi:10.1029/2008WR007615, 2009.
- 5
- 6 Badas, M. G., Deidda, R., and Piga, E.: Modulation of homogeneous space-time rainfall cascades  
7 to account for orographic influences, *Nat. Hazard Earth Sys. Sci.* 6, 427–437, 2006.
- 8
- 9 Bardossy, A., and Pegram, G.: Downscaling precipitation using regional climate models and  
10 circulations patterns toward hydrology, *Water Resour. Res.*, 47, W04505, 1-18, 2011.
- 11
- 12 Beniston M., et al.: Future extreme events in European climate: an exploration of regional  
13 climate model projections, *Climatic Change*, 81(1), 71-95, 2007.
- 14
- 15 Beven, K.: Runoff generation in semi-arid areas, in: *Dryland Rivers*, Bull LJ, Kirkby MJ (eds), J.  
16 Wiley & Sons, pp. 57–105, 2002.
- 17
- 18 Borga, M., Boscolo, P., Zanon, F., and Sangati, M.: Hydrometeorological Analysis of the 29  
19 August 2003 Flash Flood in the Eastern Italian Alps, *J. Hydrometeorol.* 8:5, 1049-1067, 2007.
- 20
- 21 Camici, S., Brocca, L., Melone, F., Moramarco, T.: Impact of climate change on flood frequency  
22 using different climate models and downscaling approaches, *J. Hydrol. Eng.*, in press,  
23 doi:10.1061/(ASCE)HE.1943-5584.0000959, 2013.
- 24
- 25 Cayan, D. R., Dasa, T., Piercea, D. W., Barnetta, T. P., Tyreea, M., and Gershunova, A.: Future  
26 dryness in the southwest US and the hydrology of the early 21st century drought, *P. Natl. Acad.*  
27 *Sci. USA*, 107, 21271-21276, doi:10.1073/pnas.0912391107, 2010.
- 28
- 29 Chessa, P. A., Cesari, D., and Delitala, A. M. S.: Mesoscale precipitation and temperature  
30 regimes in Sardinia (Italy) and their related synoptic circulation, *Theor. Appl. Climatol.*, 63,  
31 195– 221, 1999.
- 32
- 33 Christensen, J. H., Boberg, F., Christensen, O. B., Lucas-Picher, P.: On the need for bias  
34 correction of regional climate change projections of temperature and precipitation, *Geophys.*  
35 *Res. Lett.*, 35, 1-6, 2008.
- 36
- 37 Deidda, R.: Multifractal analysis and simulation of rainfall fields in space, *Phys. Chem. Earth*,  
38 24(1–2), 73–78, 1999.
- 39
- 40 Deidda, R.: Rainfall downscaling in a space-time multifractal framework, *Water Resour. Res.*,  
41 36(7), 1779–1784, 2000.
- 42
- 43 Deidda, R., Marroccu, M., Caroletti, G., Pusceddu, G., Langousis, A., Lucarini, V., Puliga, M.,  
44 and Speranza, A.: Regional climate models' performance in representing precipitation and

1 temperature over selected Mediterranean areas, *Hydrol. Earth Syst. Sci.*, 17, 5041-5059,  
2 doi:10.5194/hess-17-5041-2013.

3

4 Delrieu, G., Nicol, J., Yates, E., Kirstetter, P.-E., Creutin, J.-D., Anquetin, S., Obled, C., and  
5 Saulnier, G.-M.: The catastrophic flash-flood event of 8–9 September 2002 in the Gard region,  
6 France: a first case study for the Cévennes–Vivarais Mediterranean hydrometeorological  
7 observatory, *J. Hydrometeorol.*, 6, 34–52, 2005.

8

9 Falloon, P., and Betts, R.: Climate impacts on European agriculture and water management in  
10 the context of adaptation and mitigation—The importance of an integrated approach, *Sci. Total*  
11 *Enviro.*, 408, Issue 23, 5667-5687, <http://dx.doi.org/10.1016/j.scitotenv.2009.05.002>, 2010.

12

13 Frei, C., Schöll, R., Fukutome, S., Schmidli, J., and Vidale, P. L.: Future change of precipitation  
14 extremes in Europe: intercomparison of scenarios from regional climate models, *J. Geophys.*  
15 *Res.*, 111, D06105, doi:10.1029/2005JD005965, 2006.

16

17 Gallart, F., Llorens, P., Latron, J., and Regüés, D.: Hydrological processes and their seasonal  
18 controls in a small Mediterranean mountain catchment in the Pyrenees, *Hydrol. Earth Syst. Sci.*,  
19 6(3), 527–537, 2002.

20

21 Giorgi, F.: Climate change hot-spots, *Geophys. Res. Lett.*, 33, L08707,  
22 doi:10.1029/2006GL025734, 2006.

23

24 Giorgi, F., and Lionello, P.: Climate change projections for the Mediterranean region, *Glob.*  
25 *Planet. Change*, 63, 90–104, 2008.

26

27 Hasson, S., Lucarini, V., and Pascale, S.: Hydrological cycle over South and Southeast Asian  
28 river basins as simulated by PCMDI/CMIP3 experiments, *Earth Syst. Dynam.*, 4, 199-217,  
29 doi:10.5194/esd-4-199-2013, 2013.

30

31 Hasson, S., Lucarini, V., Pascale, S., and Böhner, J.: Seasonality of the hydrological cycle in  
32 major South and Southeast Asian river basins as simulated by PCMDI/CMIP3 experiments,  
33 *Earth Syst. Dynam.*, 5, 67-87, doi:10.5194/esd-5-67-2014, 2014.

34

35 Haylock, M. R., Hofstra, N., Klein Tank, A. M. G., Klok, E. J., Jones, P. D., and New, M.: A  
36 European daily high-resolution gridded dataset of surface temperature and precipitation, *J.*  
37 *Geophys. Res. (Atmospheres)*, 113, D20119, doi:10.1029/2008JD10201, 2008.

38

39 Hoerling, M., Eischeid, J., Perlwitz, J., Quan, X., Zhang, T., and Pegion, P.: On the Increased  
40 Frequency of Mediterranean Drought, *J. Climate*, 25, 2146–2161, doi:  
41 <http://dx.doi.org/10.1175/JCLI-D-11-00296.1>, 2012.

42

43 IPCC (Intergovernmental Panel on Climate Change), *Climate change 2007: impacts, adaptation*  
44 *and vulnerability, Contribution of Working Group II to the Fourth Assessment Report of the*  
45 *Intergovernmental Panel on Climate Change*, Cambridge University Press, Cambridge, UK, 976,  
46 2007.



1  
2 Ivanov, V. Y., Vivoni, E. R., Bras, R. L., and Entekhabi, D.: Catchment hydrologic response  
3 with a fully-distributed triangulated irregular network model, *Water Resour. Res.*, 40(11), 1–23,  
4 doi:10.1029/2004WR003218, 2004a.  
5  
6 Ivanov, V. Y., Vivoni, E. R., Bras, R. L., Entekhabi, D.: Preserving high-resolution surface and  
7 rainfall data in operational-scale basin hydrology: A fully-distributed physically-based approach,  
8 *J. Hydrol.*, 298, 80–111, doi:10.1016/j.jhydrol.2004.03.041, 2004b.  
9  
10 Liston, G. E., and Elder, K.: A Meteorological Distribution System for High-Resolution  
11 Terrestrial Modeling (Micro Met), *J. Hydrometeor.*, 7, 217-234, 2006.  
12  
13 Liuzzo, L., Noto, L. V., Vivoni, E. R., and La Loggia, G.: Basin-scale water resources  
14 assessment in Oklahoma under synthetic climate change scenarios using a fully distributed  
15 hydrological model, *J. Hydrol. Eng.*, 15(2), 107–122, doi:10.1061/ASCEHE.1943-  
16 5584.0000166, 2010.  
17  
18 Lucarini, V., Danihlik, R., Kriegerova, I., and Speranza, A.: Does the Danube exist? Versions of  
19 reality given by various regional climate models and climatological data sets, *J. Geophys. Res.*,  
20 112, D13103, doi:10.1029/2006JD008360, 2007.  
21  
22 Lucarini, V., Danihlik, R., Kriegerova, I., and Speranza, A.: Hydrological cycle in the Danube  
23 basin in present-day and XXII century simulations by IPCCAR4 global climate models, *J.*  
24 *Geophys. Res.*, 113, D09107, doi:10.1029/2007JD009167, 2008.  
25  
26 Lucarini, V.: Validation of climate models, in: *Encyclopaedia of Global Warming and Climate*  
27 *Change*, edited by: Philander, G., SAGE, Thousand Oaks, USA, 1053–1057, 2008  
28  
29 Ludwig, R., et al.: Climate-induced changes on the hydrology of Mediterranean basins - A  
30 research concept to reduce uncertainty and quantify risk, *Fresen. Environ. Bull.*, 19 (10 A),  
31 2379–2384, 2010.  
32  
33 Mahfouf, J. F., and Noilhan, J.: Comparative study of various formulations from bare soil using  
34 in situ data, *J. Appl. Meteorol.*, 30, 1354–1365, 1991.  
35  
36 Mahmood, T. H., and Vivoni, E. R.: Forest ecohydrological response to bimodal precipitation  
37 during contrasting winter to summer transitions, *Ecohydrology*, (In Press), 2014.  
38  
39 Maraun, F., Wetterhall, A. M., Ireson, R. E., Chandler, E. J., Kendon, M., Widmann, S., Brienen,  
40 H. W., Rust, T., Sauter, M., Themeßl, V. K. C., Venema, K. P., Chun, C. M., Goodess, R. G.,  
41 Jones, C., Onof, M., Vrac, I., and Thiele-Eich: Precipitation downscaling under climate change.  
42 Recent developments to bridge the gap between dynamical models and the end user, *Rev.*  
43 *Geophys.*, 48, RG3003, doi:10.1029/2009RG000314, 2010.  
44  
45 Mariotti, A.: Recent changes in the Mediterranean water cycle: A pathway toward long-term  
46 regional hydroclimatic change?, *J. Climate*, 23, 1513–1525, 2010.

1  
2 Mariotti, A., Zeng, N., Yoon, J.-H., Artale, V., Navarra, A., Alpert, P., and Li, L. Z. X.:  
3 Mediterranean water cycle changes: Transition to drier 21st century conditions in observations  
4 and CMIP3 simulations, *Environ. Res. Lett.*, 3, 044001, doi:10.1088/1748-9326/3/4/044001,  
5 2008.  
6  
7 Mascaro, G., Vivoni, E. R., and Deidda, R.: Implications of ensemble quantitative precipitation  
8 forecast errors on distributed streamflow forecasting, *J. Hydrometeorol.*, 11(1), 69–86,  
9 doi:10.1175/2009JHM1144.1, 2010.  
10  
11 Mascaro, G., Piras, M., Deidda, R., and Vivoni, E. R.: Distributed hydrologic modeling of a  
12 sparsely monitored basin in Sardinia, Italy, through hydrometeorological downscaling, *Hydrol.*  
13 *Earth Syst. Sci.*, 17, 4143–4158, doi:10.5194/hess-17-4143-2013, 2013a.  
14  
15 Mascaro, G., Deidda, R., and Hellies, M.: On the nature of rainfall intermittency as revealed by  
16 different metrics and sampling approaches, *Hydrol. Earth Syst. Sci.*, 17, 355–369,  
17 doi:10.5194/hess-17-355-2013, 2013b.  
18  
19 Maurer, E. P., and Hidalgo, H. G.: Utility of daily vs. monthly large-scale climate data: an  
20 intercomparison of two statistical downscaling methods, *Hydrol. Earth Syst. Sci.*, 12, 551–563,  
21 doi:10.5194/hess-12-551-2008, 2008.  
22  
23 Montenegro, S., and Ragab, R.: Impact of possible climate and land use changes in the semi arid  
24 regions: a case study from North Eastern Brazil, *J. Hydrol.*, 434-435, 55–68,  
25 doi:10.1016/j.jhydrol.2012.02.036, 2012.  
26  
27 Moreno, H. A., Vivoni, E. R., and Gochis, D. J.: Limits to flood forecasting in the Colorado  
28 Front Range for two summer convection periods using radar nowcasting and a distributed  
29 hydrologic model, *J. Hydrometeorol.*, 14(4), 1075-1097, 2013.  
30  
31 Moussa, R., Chahinian, N., and Bocquillon, C.: Distributed hydrological modeling of a  
32 Mediterranean mountainous catchment – model construction and multi-site validation, *J.*  
33 *Hydrol.*, 337, 35–51, doi:10.1016/j.jhydrol.2007.01.028, 2007.  
34  
35 Nakićević, N., Alcamo, J., Davis, G., de Vries, H. J. M., Fenhann, J., Gaffin, S., Gregory, K.,  
36 Grubler, A., Jung, T. Y., Kram, T., La Rovere, E. L., Michaelis, L., Mori, S., Morita, T., Papper,  
37 W., Pitcher, H., Price, L., Riahi, K., Roehrl, A., Rogner, H-H., Sankovski, A., Schlesinger, M.,  
38 Shukla, P., Smith, S., Swart, R., van Rooijen, S., Victor, N., and Dadi, Z.: Emissions Scenarios.  
39 A Special Report of Working Group III of the Intergovernmental Panel on Climate Change.  
40 Cambridge University Press: Cambridge; 559, 2000.  
41  
42 Olesen, J. E., and Bindi, M.: Consequences of climate change for European agricultural  
43 productivity, land use and policy, *Eur. J. Agron.*, 16, 239–262, 2002.  
44

1 Piñol, J., Beven, K., and Freer, J.: Modelling the hydrological response of Mediterranean  
2 catchments, Prades, Catalonia. The use of distributed models as aids to hypothesis formulation,  
3 Hydrol. Process., 11, 1287–1306, 1997.  
4  
5 Pulina, M. A.: L'Evapotraspirazione potenziale in Sardegna in funzione dello studio del regime  
6 idrico dei suoli. Studi sassaresi: organo ufficiale della Società sassarese di Scienze mediche e  
7 naturali, Sez. 3: Annali della Facoltà di Agraria dell'Università di Sassari, Vol. 32, 96–109, ISSN  
8 0562-2662, 1986.  
9  
10 Senatore, A., Mendicino, G., Smiatek, G., and Kunstmann, H.: Regional climate change  
11 projections and hydrological impact analysis for a Mediterranean basin in Southern Italy, J.  
12 Hydrol., 399, 70-92, 2011.  
13  
14 Silvestro, F., Gabellani, S., Giannoni, F., Parodi, A., Rebora, N., Rudari, R., and Siccardi, F.: A  
15 hydrological analysis of the 4 November 2011 event in Genoa, Nat. Hazard Earth Sys. Sci., 12,  
16 2743–2752, 2012.  
17  
18 Sulis, M., Paniconi, C., Rivard, C., Harvey, R., and Chaumont, D.: Assessment of climate change  
19 impacts at the catchment scale with a detailed hydrological model of surface-subsurface  
20 interactions and comparison with a land surface model, Water Resour. Res., 47, W01513,  
21 doi:10.1029/2010WR009167, 2011.  
22  
23 Sulis, M., Paniconi, C., Marroccu, M., Huard, D., and Chaumont, D.: Hydrologic response to  
24 multimodel climate output using a physically based model of groundwater/surface water  
25 interactions, Water Resour. Res., 48, W12510, doi:10.1029/2012WR012304, 2012.  
26  
27 Tramblay, Y., Ruelland, D., Somot, S., Bouaicha, R., and Servat, E.: High-resolution Med-  
28 CORDEX regional climate model simulations for hydrological impact studies: a first evaluation  
29 of the ALADIN-Climate model in Morocco, Hydrol. Earth Syst. Sci., 17, 3721-3739  
30 <http://dx.doi.org/10.5194/hess-17-3721-2013>, 2013.  
31  
32 Vivoni, E. R., Ivanov, V. Y., Bras, R. L., and Entekhabi, D.: Generation of triangulated irregular  
33 networks based on hydrological similarity, J. Hydrol. Eng., 9(4), 288–302,  
34 doi:10.1061/ASCE1084-0699(2004)9:4(288), 2004.  
35  
36 Vivoni, E. R., Ivanov, V. Y., Bras, R. L., and Entekhabi, D.: On the effects of triangulated terrain  
37 resolution on distributed hydrologic model response, Hydrol. Process., 19(11), 2101–2122,  
38 doi:10.1002/hyp.5671, 2005.  
39  
40 Vivoni, E. R., Mascaro, G., Mniszewski, S., Fasel, P., Springer, E. P., Ivanov, V. Y. and Bras, R.  
41 L.: Real-world hydrologic assessment of a fully-distributed hydrological model in a parallel  
42 computing environment, J. Hydrol., 409, 483–496, doi:10.1016/j.jhydrol.2011.08.053, 2011.  
43  
44 Wilby, R. L., and Wigley, T. M. L.: Downscaling general circulation model output: A review of  
45 methods and limitations, Prog. Phys. Geogr., 21, 530–548, 1997.  
46

- 1 Wood, A. W., Leung, L. R., Sridhar, V., and Lettenmaier, D. P.: Hydrologic implications of
- 2 dynamical and statistical approaches to downscaling climate model outputs, *Climatic Change*,
- 3 62, 189–216, 2004.

1 **Table Captions**

2 **Table 1.** List of the Global Climate Models (GCMs) used as drivers of ENSEMBLES Regional  
3 Climate Models (RCMs) considered in this study together with corresponding climatological  
4 center and model, and acronyms adopted. The four GCM-RCM combinations used in this study  
5 are ECH-RCA, ECH-REM, ECH-RMO and HCH-RCA.

6  
7 **Table 2.** Mean annual values of MAP,  $T$  and  $Q$  in the RMB in REF and FUT periods with  
8 relative changes for each CM. The mean and standard deviation (Std) are also reported.

9  
10 **Table 3.** Terrain, soil texture and land cover characteristics of the RMB sub-basins shown in Fig.  
11 2b, including: contributing area ( $A_c$ ), slope, and length of the main channel ( $L$ ); percentages of  
12 Sandy loam - Sandy clay loam (SL-SCL), Clay loam – Clay (CL-C), Sandy loam – Loam (SL-  
13 L); and percentages of Agriculture (A), Sparse Vegetation (SV), and Olives (O).

14  
15

	<b>Climatological center and model</b>	<b>Acronym</b>
Global Climate Models, GCMs	Hadley Centre for Climate Prediction, Met Office, UK HadCM3 Model	HCH
	Max Planck Institute for Meteorology, Germany ECHAM5 / MPI Model	ECH
Regional Climate Models, RCMs	Swedish Meteorological and Hydrological Institute (SMHI), Sweden RCA Model	RCA
	Max Planck Institute for Meteorology, Hamburg, Germany REMO Model	REM
	Koninklijk Nederlands Meteorologisch Instituut (KNMI), Netherlands RACMO2 Model	RMO

1  
2  
3  
4  
5  
6  
7

**Table 1.** List of the Global Climate Models (GCMs) used as drivers of ENSEMBLES Regional Climate Models (RCMs) considered in this study together with corresponding climatological center and model, and acronyms adopted. The four GCM-RCM combinations used in this study are ECH-RCA, ECH-REM, ECH-RMO and HCH-RCA.

Climate Model Combination	Mean annual MAP			Mean annual $T$			Mean annual $Q$		
	REF (mm)	FUT (mm)	$\Delta$ MAP (%)	REF (°C)	FUT (°C)	$\Delta T$ (°C)	REF (mm)	FUT (mm)	$\Delta Q$ (%)
ECH-RCA	570.93	502.81	-11.93	16.85	18.72	1.87	107.39	71.90	-33.05
ECH-REM	559.71	519.18	-7.24	16.77	18.68	1.91	86.74	71.87	-17.14
ECH-RMO	542.80	487.87	-10.12	16.83	18.72	1.89	91.30	67.87	-25.66
HCH-RCA	575.06	453.19	-21.19	16.52	19.59	3.08	107.96	53.71	-50.24
Mean	562.13	490.76	-12.70	16.74	18.93	2.18	98.35	66.34	-32.55
Std	14.42	28.12	6.03	0.15	0.44	0.60	10.93	8.63	14.07

1

2 **Table 2.** Mean annual values of MAP,  $T$  and  $Q$  in the RMB in REF and FUT periods with  
3 relative changes for each CM. The mean and standard deviation (Std) are also reported.

4

Sub-basin	$A_c$ (km <sup>2</sup> )	Slope (%)	$L$ (km)	Main soil texture classes			Main land cover classes		
				SL-SCL	CL-C	SL-L	A	SV	O
1	28.00	10.43	14.60	9.35	88.33	0.00	87.01	7.21	0.84
2	14.82	9.03	7.15	5.05	89.98	0.00	71.81	3.48	17.34
3	50.17	8.96	16.55	7.44	89.02	0.00	82.38	5.31	5.71
4	10.78	5.56	8.09	17.40	77.35	0.00	90.83	0.00	4.44
5	68.10	13.79	18.36	18.72	60.89	15.98	67.74	10.46	6.77
6	42.67	22.93	16.51	3.37	26.98	69.05	31.33	39.13	5.82
7	113.51	16.98	20.06	12.79	49.09	34.89	54.20	20.70	6.69
8	20.95	16.59	13.55	0.00	58.55	31.52	30.34	25.43	16.77
9	70.16	7.70	19.55	8.09	88.09	0.00	84.90	4.12	5.31
10	135.01	16.89	21.07	10.85	50.38	34.38	50.68	21.43	8.16
11	11.54	7.46	8.11	23.14	65.28	0.00	74.95	7.07	4.02
12	221.99	13.71	27.40	11.46	60.65	21.49	60.65	16.19	7.67
13	244.99	13.14	30.55	13.30	60.05	19.60	61.96	15.40	7.26
14	58.18	19.05	22.43	21.42	3.28	42.32	25.05	47.24	8.86
15	41.99	33.82	13.43	0.81	0.00	93.06	4.70	67.23	0.00
16	23.96	34.58	10.76	5.57	0.09	94.18	2.44	74.56	4.35
17	315.75	13.77	34.77	15.83	48.48	23.39	55.95	20.67	7.41
18	436.41	16.67	25.45	19.25	35.63	34.06	45.39	28.16	8.54
19	28.59	6.35	15.09	27.73	58.31	0.77	76.55	2.35	4.53
20-Outlet	472.50	17.30	38.75	19.61	36.67	31.91	47.43	26.38	8.21

1  
2 **Table 3.** Terrain, soil texture and land cover characteristics of the RMB sub-basins shown in Fig.  
3 2b, including: contributing area ( $A_c$ ), slope, and length of the main channel ( $L$ ); percentages of  
4 Sandy loam –Sandy clay loam (SL-SCL), Clay loam –Clay (CL-C), Sandy loam –Loam (SL-L);  
5 and percentages of Agriculture (A), Sparse Vegetation (SV), and Olives (O).

6



## 1 **Figure Captions**

2 **Fig. 1.** Location of the RMB within (a) Italy and (b) the island of Sardinia. (c) DEM of the RMB  
3 in UTM coordinates. In (b) and (c), crosses are centroids of the 25-km grid of the RCMs, and the  
4 black square is the 104-km x 104-km coarse-scale domain for the precipitation downscaling  
5 scheme. In (c), the circles are the centroids of the 5-km grid of the disaggregated precipitation  
6 products, and the triangles are the rain gages used to perform the local-scale bias correction.

7  
8 **Fig. 2.** (a) Land cover and (b) soil texture maps used as input for the tRIBS model. In (b), the  
9 boundaries of 20 sub-basins are also reported along with the stream network.

10  
11 **Fig. 3.** Illustration of the local-scale bias correction. Black line: climatological monthly average  
12 of the mean areal precipitation (MAP) in the RMB observed by 13 rain gages over 1951-2008.  
13 Black dashed line: MAP averaged across the four CMs during the same period before the bias  
14 correction. Gray shades continuous lines: MAP of the four CMs after removing the bias.

15  
16 **Fig. 4.** (a) Mean monthly MAP in the RMB in REF (black) and FUT (gray). Bars are mean  $\pm$   
17 standard deviation across the CMs. (b) Relative change between FUT and REF periods in mean  
18 monthly MAP ( $\Delta$ MAP). (c)-(d) Same as (a)-(b), but for the mean monthly  $N$ . (e)-(f) Same as (a)-  
19 (b), but for the mean monthly  $I$ .

20  
21 **Fig. 5.** Same as Fig. 4, but for the mean monthly  $T$ .

22  
23 **Fig. 6.** Same as Fig. 4, but for the mean monthly  $Q$  at the RMB outlet.

24  
25 **Fig. 7.** (a) Relation between the change in annual runoff,  $\Delta Q$ , and sub-basin contributing area,  
26  $A_c$ . (b) Relation between the mean level of the groundwater table,  $N_{wt}$ , in the FUT period and  $A_c$ .

1 Bars represent mean  $\pm$  standard deviation across the CMs. The number of each sub-basin as  
2 reported in Fig. 2b and Table 3 is also indicated.

3  
4 **Fig. 8.** (a) Partitioning of  $Q$  at the RMB outlet in the REF period among the four runoff  
5 generation mechanisms: infiltration excess ( $Q_{IE}$ ), saturation excess ( $Q_{SE}$ ), perched return flow  
6 ( $Q_{PR}$ ), and groundwater exfiltration ( $Q_{GE}$ ) runoff components. (b)  $\Delta Q$  for the runoff mechanisms.

7  
8 **Fig. 9.** FDCs computed from the discharge at the RMB outlet. Continuous (dashed) lines are  
9 used for REF (FUT). Circle shows the threshold discharge,  $Q_{LF}$ , used to identify low flow  
10 conditions.

11  
12 **Fig. 10.** (a) Mean monthly number of low flow days (LFDs) in REF (black) and FUT (gray).  
13 Bars are mean  $\pm$  standard deviation across the CMs. (b) Mean annual maximum consecutive  
14 length of LFDs in REF (black) and FUT (gray) periods.

15  
16 **Fig. 11.** Relation between the change in the mean of the annual maximum  $Q$ ,  $\Delta\mu_q$ , and the  
17 corresponding mean slope. Black (gray) circles indicate sub-basins dominated by the Clay loam  
18 – Clay (Sandy loam – Loam) class; a cross is used to indicate sub-basins 1-4 and 9. Each panel  
19 refers to results obtained for each CM.

20  
21 **Fig. 12.** (a) Mean monthly  $ET_0$  (dashed lines) and  $ET_a$  (continuous lines) plotted as mean  $\pm$   
22 standard deviation of the four CMs in REF (black) and FUT (gray); (b) Mean across the CMs of  
23 the relative changes of  $ET_0$ ,  $ET_a$ , and  $SWC$ .

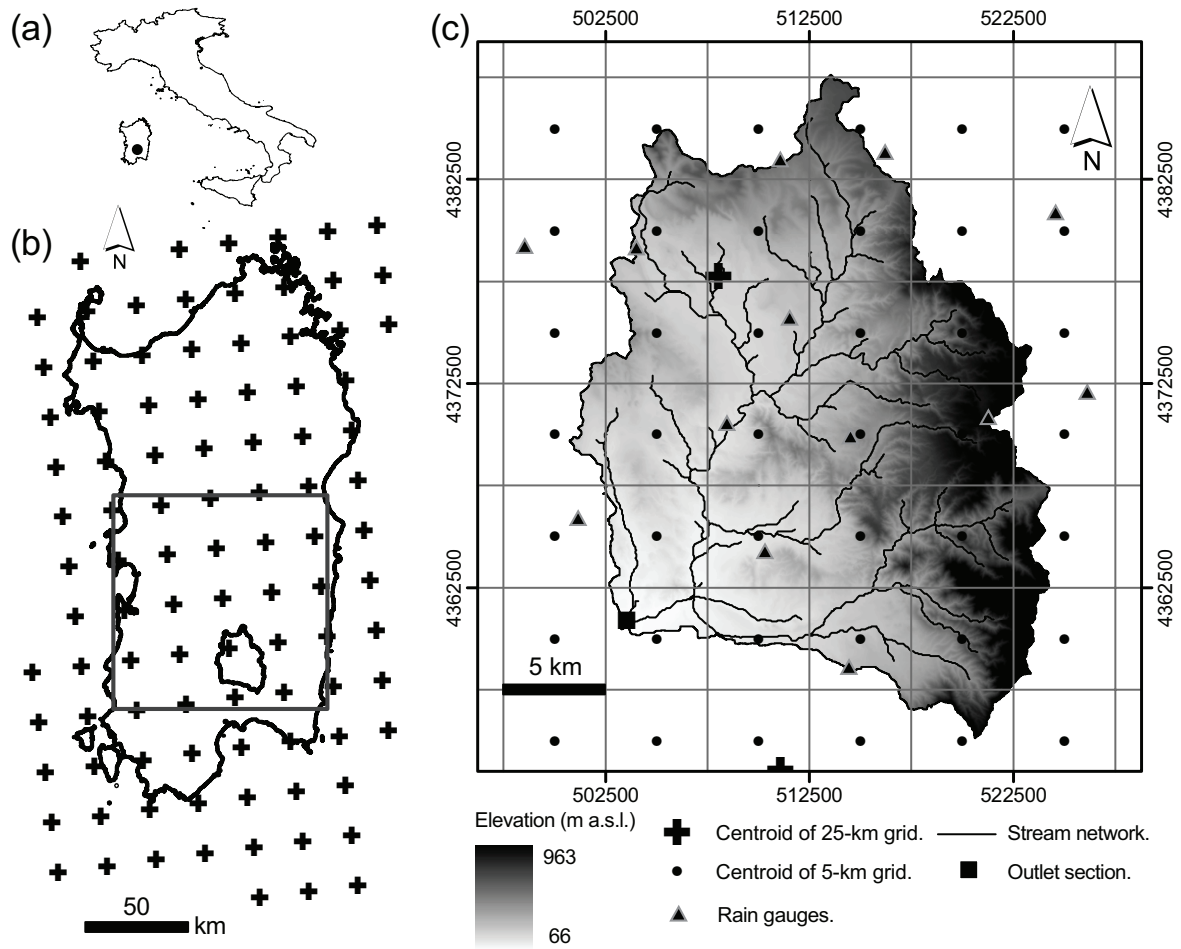
24  
25 **Fig. 13.** Changes between REF and FUT periods averaged over the winter season (December-  
26 February) for (a)  $P$ , (b)  $SWC$ , (c)  $ET_0$ , and (d)  $ET_a$  under the ECH-RCA combination. In (b),

1 areas where the variables are characterized by positive or lower negative changes are indicated  
2 with L, while regions with higher negative changes are indicated with H.

3  
4 **Fig. 14.** Same as Fig. 13, but for the spring season.

5

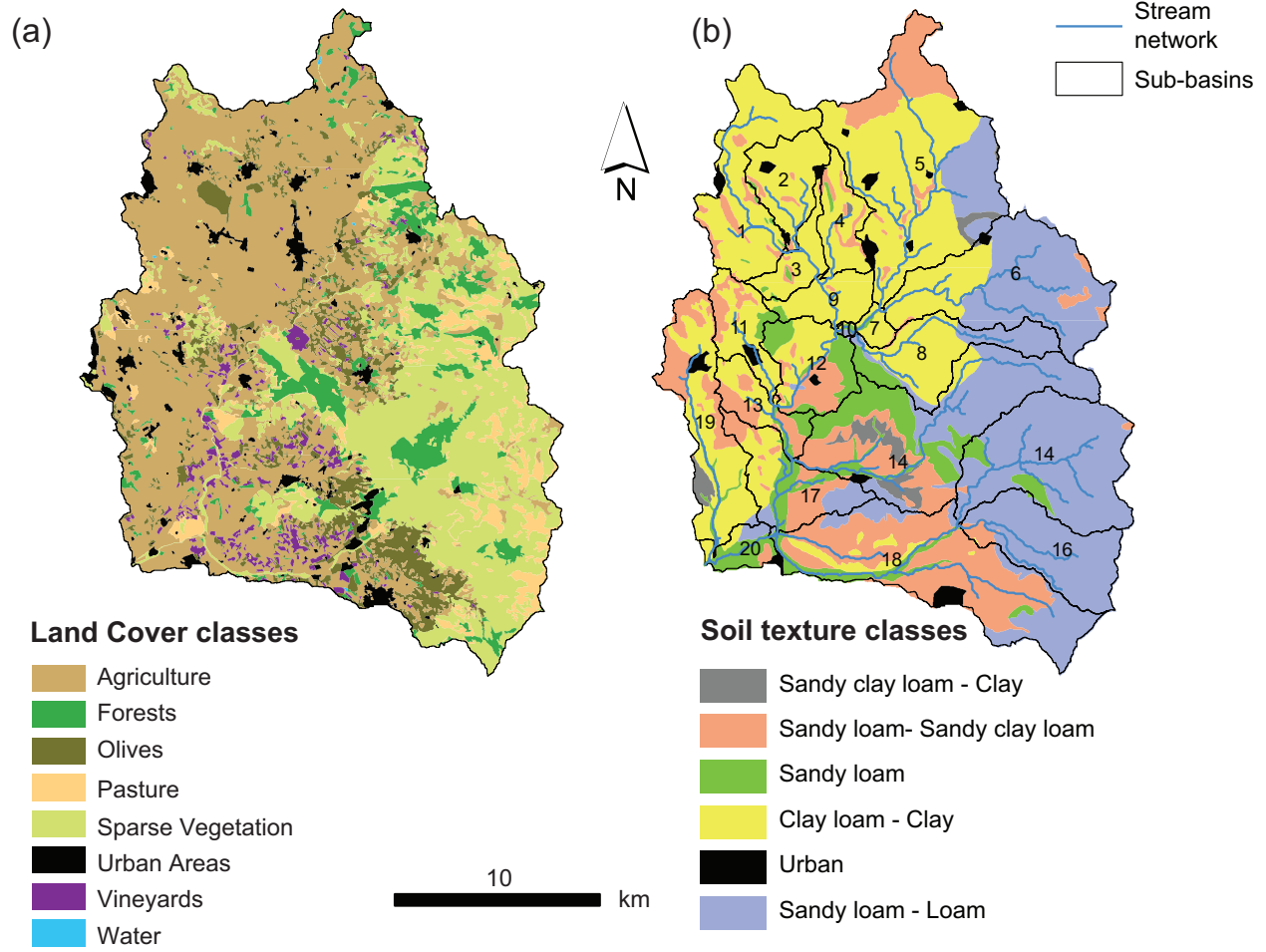
6



1  
2

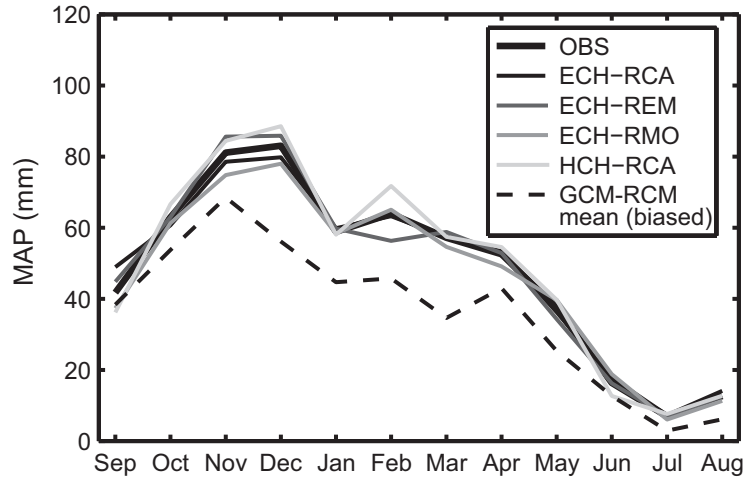
3 **Fig. 1.** Location of the RMB within (a) Italy and (b) the island of Sardinia. (c) DEM of the RMB  
 4 in UTM coordinates. In (b) and (c), crosses are the centroids of the 25-km grid of the RCMs, and  
 5 the black square is the 104-km x 104-km coarse-scale domain for the precipitation downscaling  
 6 scheme. In (c), the circles are the centroids of the 5-km grid of the disaggregated precipitation  
 7 products, and the triangles are the rain gauges used to perform the local-scale bias correction.

8



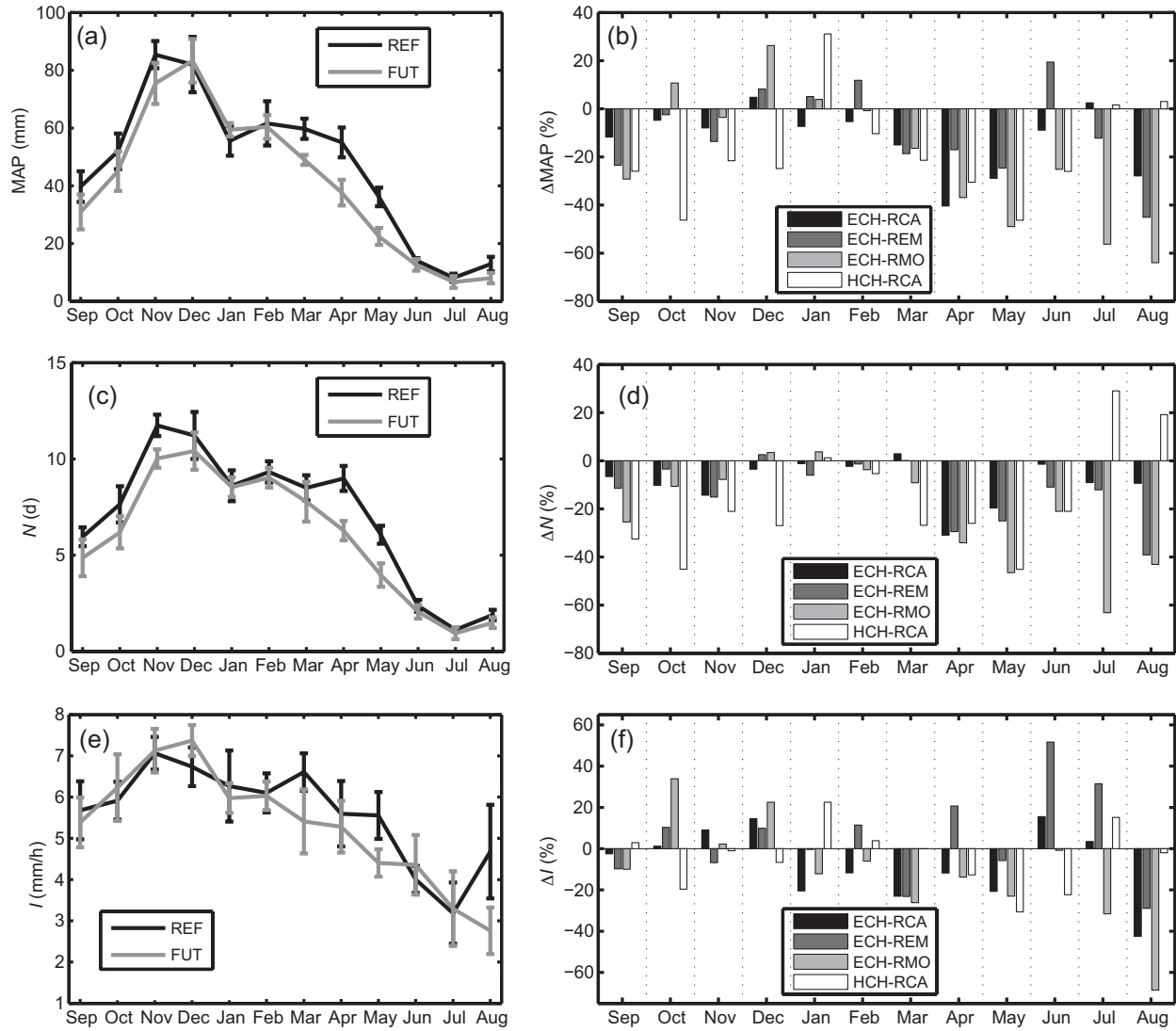
1  
2  
3  
4  
5

**Fig. 2.** (a) Land cover and (b) soil texture maps used as input for the tRIBS model. In (b), the boundaries of 20 sub-basins are also reported along with the stream network.



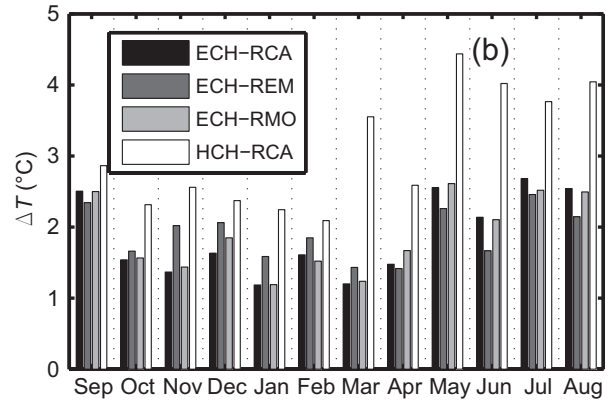
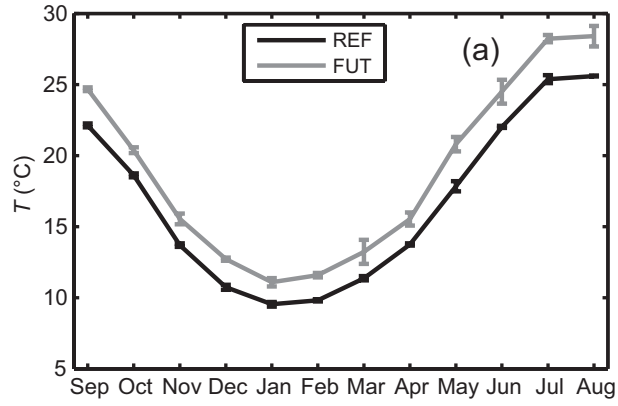
1  
2  
3  
4  
5  
6  
7

**Fig. 3.** Illustration of the local-scale bias correction. Black line: climatological monthly average of the mean areal precipitation (MAP) in the RMB observed by 13 rain gages over 1951-2008. Black dashed line: MAP averaged across the four CMs during the same period before the bias correction. Gray shades continuous lines: MAP of the four CMs after removing the bias.



1  
2 **Fig. 4.** (a) Mean monthly MAP in the RMB in REF (black) and FUT (gray). Bars are mean  $\pm$   
3 standard deviation across the CMs. (b) Relative change between FUT and REF periods in mean  
4 monthly MAP ( $\Delta$ MAP). (c)-(d) Same as (a)-(b), but for the mean monthly  $N$ . (e)-(f) Same as (a)-  
5 (b), but for the mean monthly  $I$ .

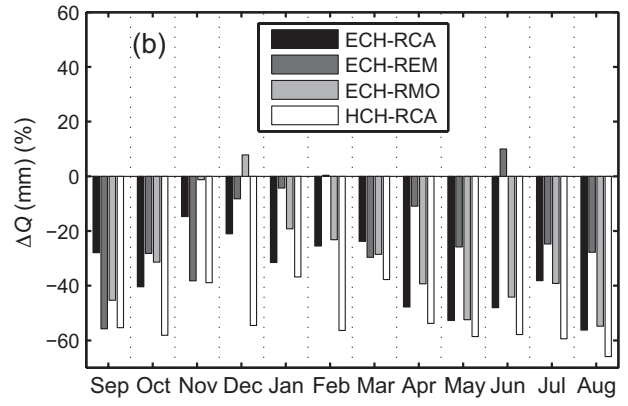
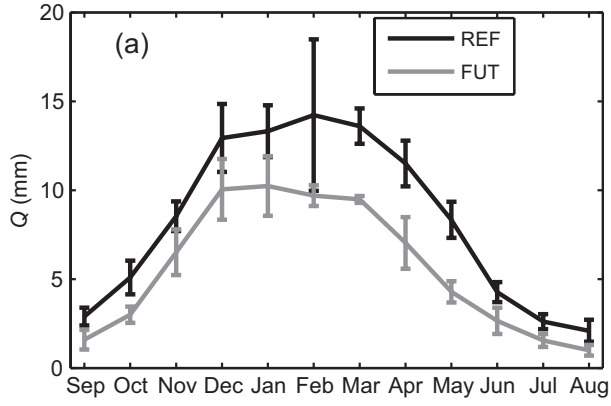
6



1  
2  
3  
4  
5

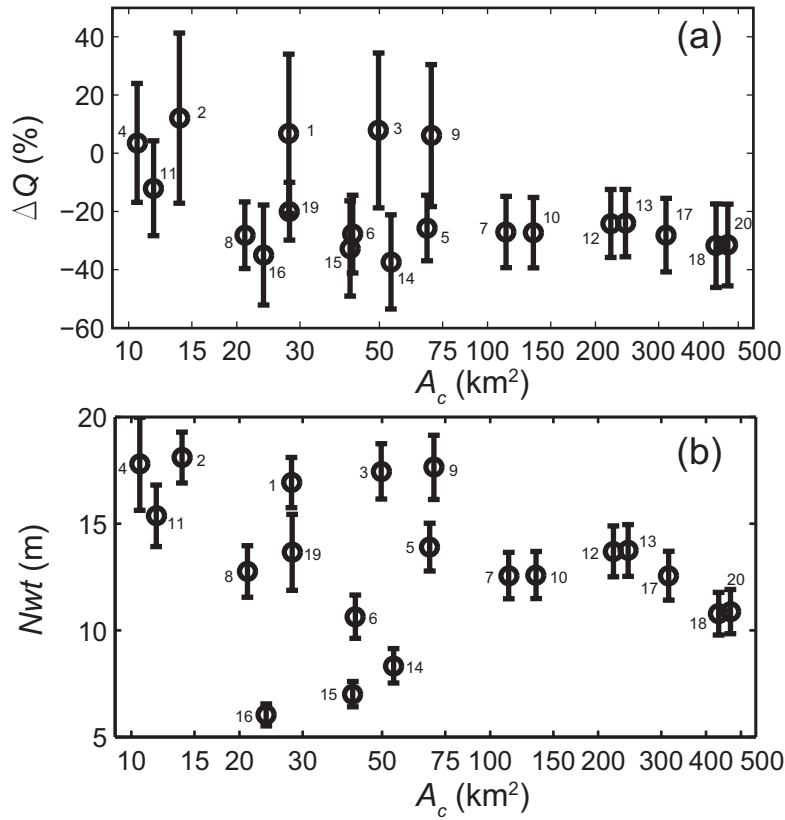
**Fig. 5.** Same as Fig. 4, but for the mean monthly  $T$ .





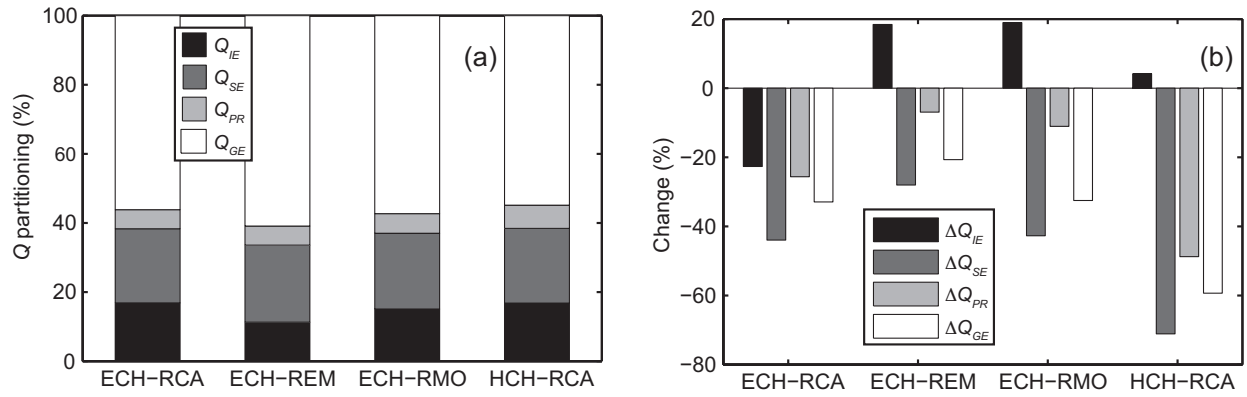
1  
2  
3  
4

**Fig. 6.** Same as Fig. 4, but for the mean monthly  $Q$  at the RMB outlet.



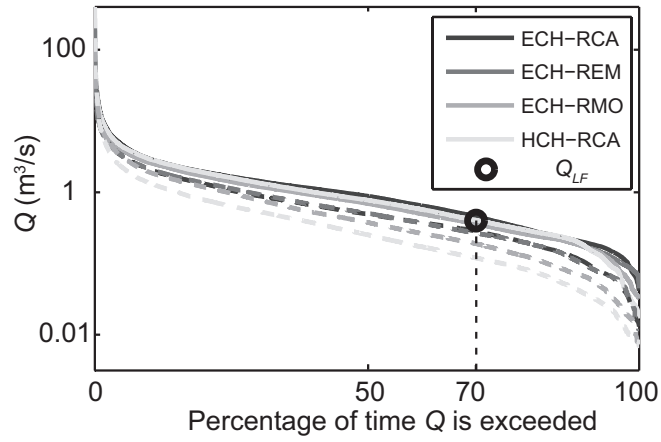
1  
2  
3 **Fig. 7.** (a) Relation between the change in annual runoff,  $\Delta Q$ , and sub-basin contributing area,  
4  $A_c$ . (b) Relation between the mean level of the groundwater table,  $Nwt$ , in the FUT period and  $A_c$ .  
5 Bars represent mean  $\pm$  standard deviation across the CMs. The number of each sub-basin as  
6 reported in Fig. 2b and Table 3 is also indicated.

7



1  
2  
3  
4  
5  
6

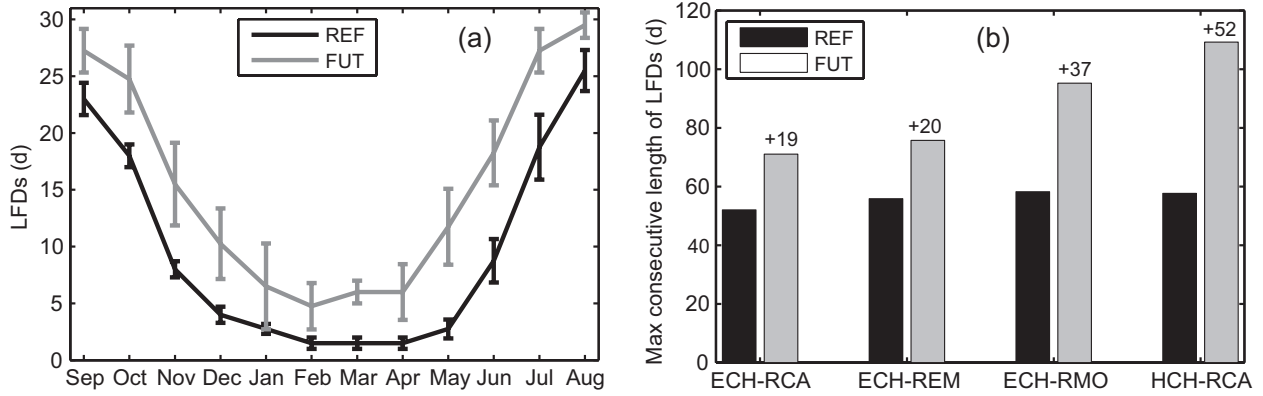
**Fig. 8.** (a) Partitioning of  $Q$  at the RMB outlet in the REF period among the four runoff generation mechanisms: infiltration excess ( $Q_{IE}$ ), saturation excess ( $Q_{SE}$ ), perched return flow ( $Q_{PR}$ ), and groundwater exfiltration ( $Q_{GE}$ ) runoff components. (b)  $\Delta Q$  for the runoff mechanisms.



1  
2

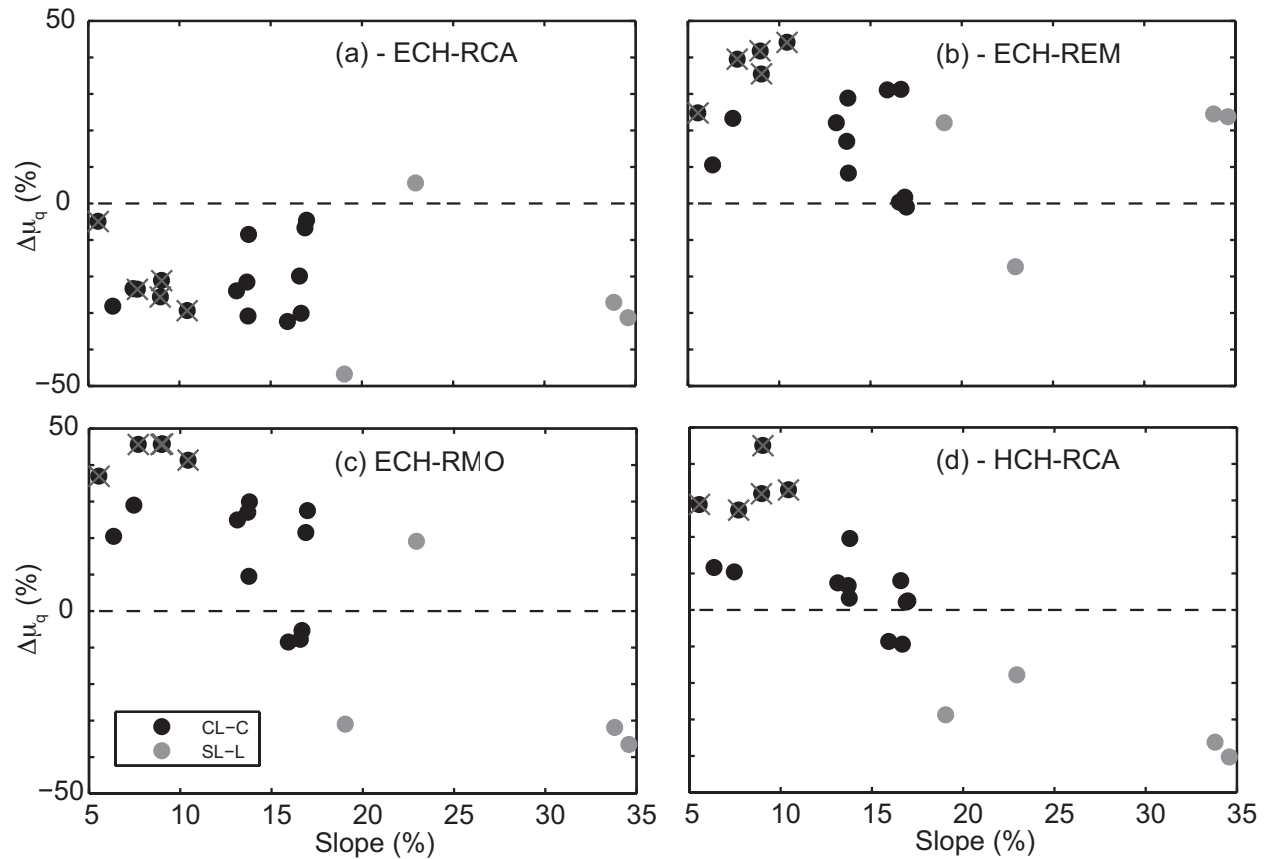
3 **Fig. 9.** FDCs computed from the discharge at the RMB outlet. Continuous (dashed) lines are  
 4 used for REF (FUT). Circle shows the threshold discharge,  $Q_{LF}$ , used to identify low flow  
 5 conditions.

6



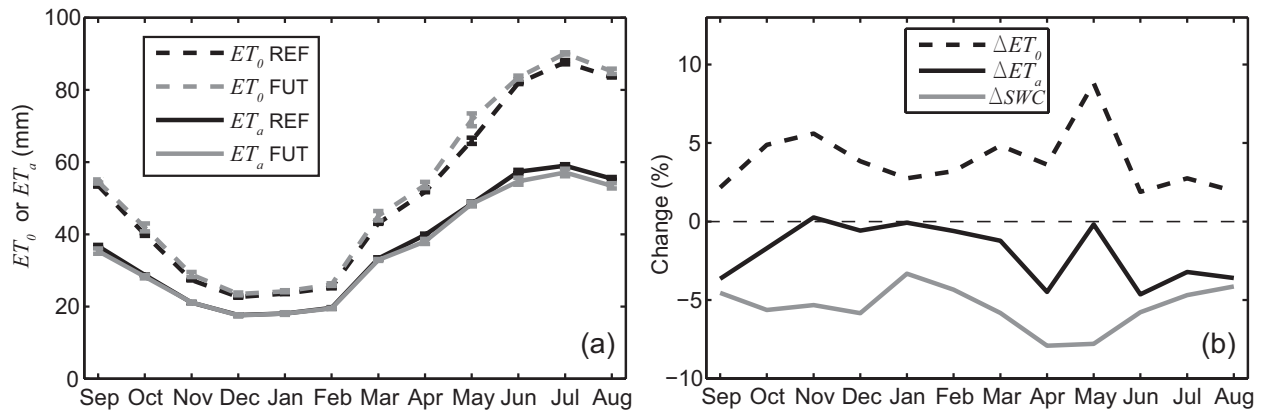
1  
2  
3  
4  
5  
6

**Fig. 10.** (a) Mean monthly number of low flow days (LFDs) in REF (black) and FUT (gray). Bars are mean  $\pm$  standard deviation across the CMs. (b) Mean annual maximum consecutive length of LFDs in REF (black) and FUT (gray) periods.



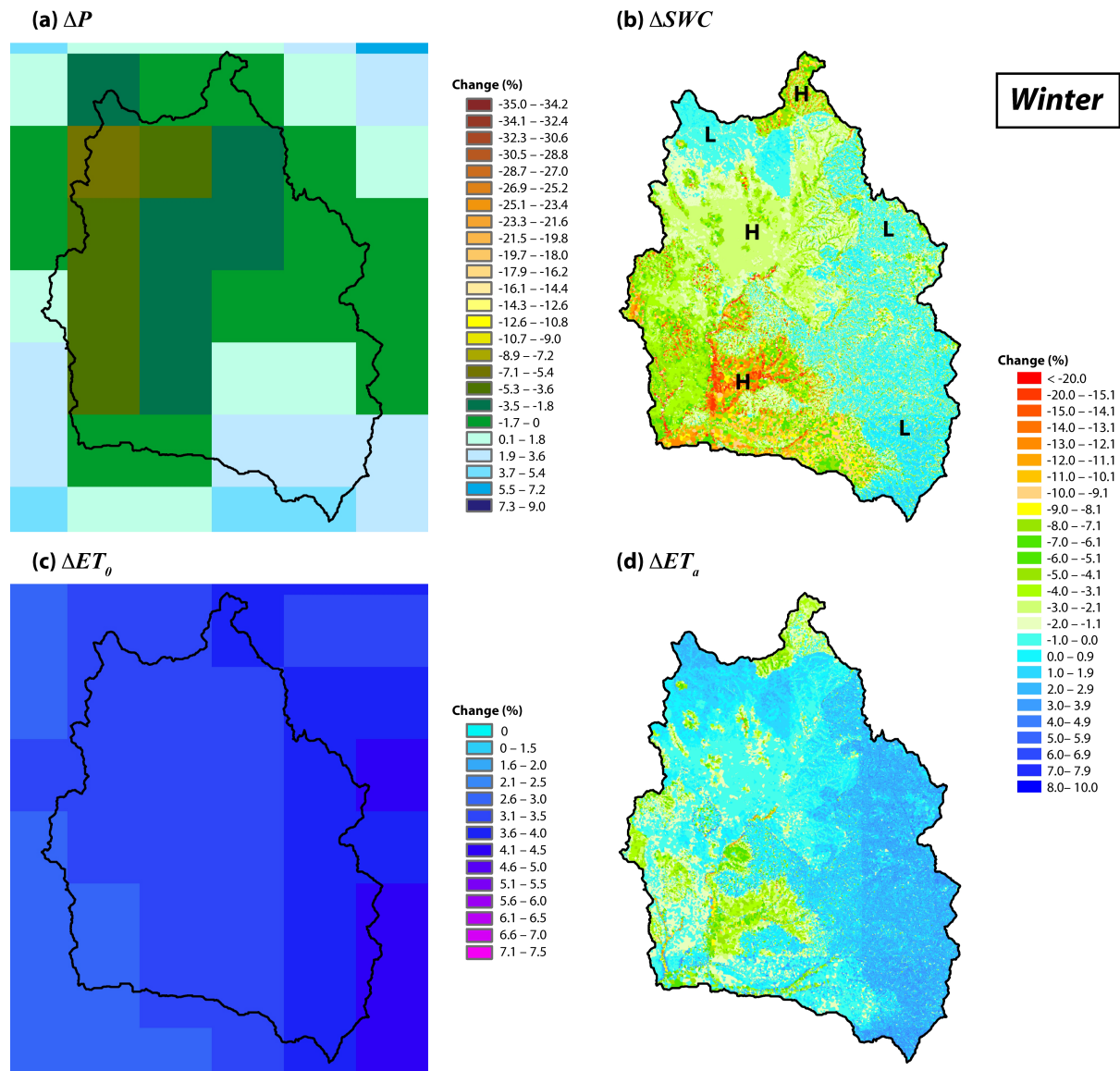
1  
2  
3  
4  
5  
6  
7  
8

**Fig. 11.** Relation between the change in the mean of the annual maximum  $Q$ ,  $\Delta\mu_q$ , and the corresponding mean slope. Black (gray) circles indicate sub-basins dominated by the Clay loam – Clay (Sandy loam – Loam) class; a cross is used to indicate sub-basins 1-4 and 9. Each panel refers to results obtained for each CM.



1  
 2 **Fig. 12.** (a) Mean monthly  $ET_0$  (dashed lines) and  $ET_a$  (continuous lines) plotted as mean  $\pm$   
 3 standard deviation of the four CMs in REF (black) and FUT (gray); (b) Mean across the CMs of  
 4 the relative change of  $ET_0$ ,  $ET_a$ , and  $SWC$ .

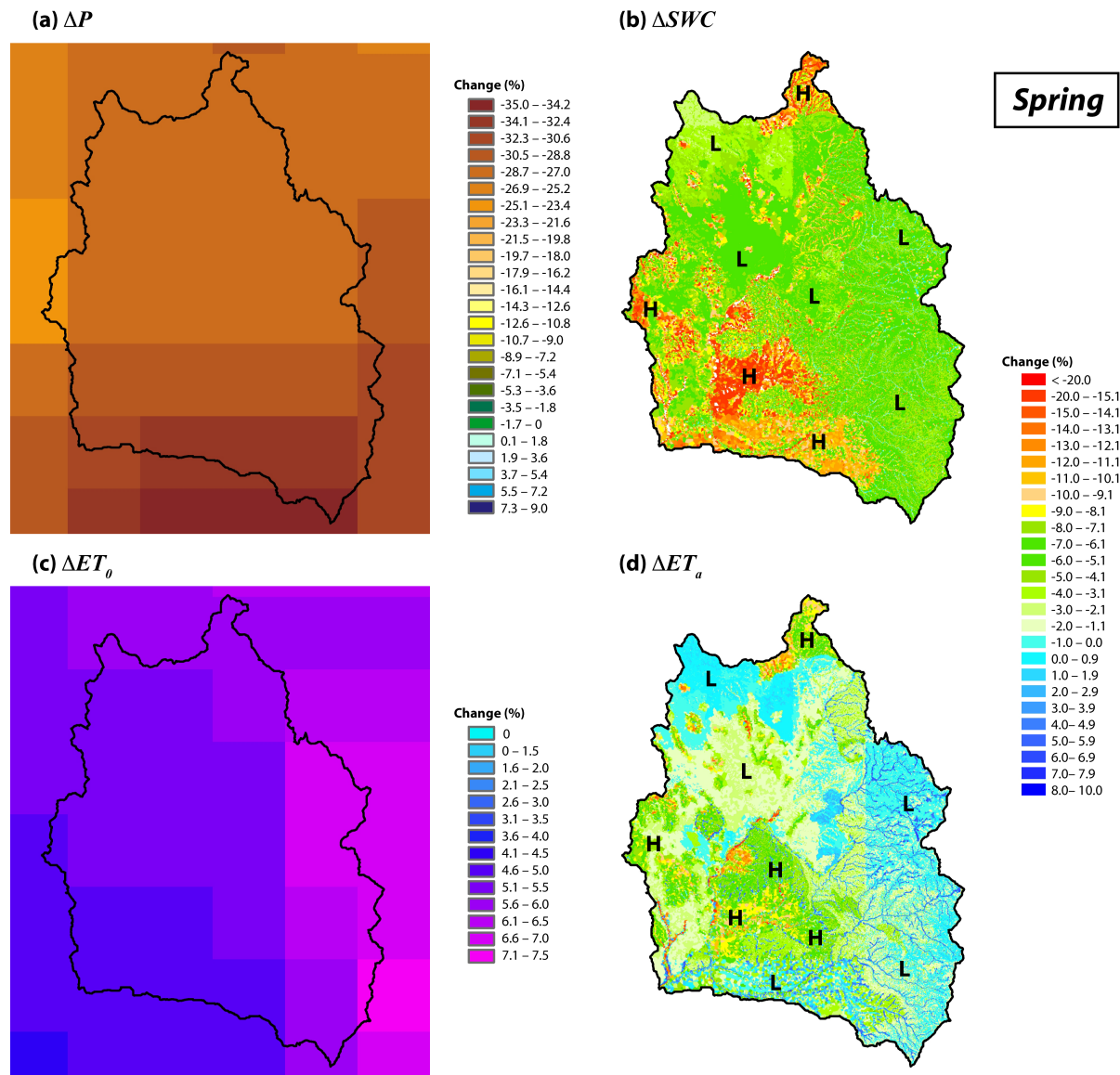
5



1  
2  
3 **Fig. 13.** Changes between REF and FUT periods averaged over the winter season (December-  
4 February) for (a)  $P$ , (b)  $SWC$ , (c)  $ET_0$ , and (d)  $ET_a$  under the ECH-RCA combination. In (b),  
5 areas where the variables are characterized by positive or lower negative changes are indicated  
6 with L, while regions with higher negative changes are indicated with H.

7





1  
2  
3 **Fig. 14.** Same as Fig. 13, but for the spring season.